

NMR LINE SHAPES AND KNIGHT SHIFTS OF  
 $\text{Na}_x\text{CoO}_{2-y}\text{H}_2\text{O}$

NMR LINE SHAPES AND KNIGHT SHIFTS OF  $\text{Na}_x\text{CoO}_2-y\text{H}_2\text{O}$

By

FANLONG NING, M. Sc.

A Thesis

Submitted to the School of Graduate Studies

in Partial Fulfilment of the Requirements

for the Degree

Master of Science

McMaster University

© Copyright by Fanlong Ning, December 2005

MASTER OF SCIENCE (2005)  
(Physics and Astronomy)

McMaster University  
Hamilton, Ontario

TITLE: NMR LINE SHAPES AND KNIGHT SHIFTS OF  
 $\text{Na}_x\text{CoO}_2-y\text{H}_2\text{O}$

AUTHOR: Fanlong Ning, M. Sc.  
Jilin University  
Changchun, P. R. China, 2003

SUPERVISOR: Dr. Takashi Imai

NUMBER OF PAGES: xi, 56

# Abstract

We investigated the local electronic properties of the triangular-lattice materials  $\text{Na}_x\text{CoO}_2$  ( $x = 0.3, 0.72$ ) and the superconductor  $\text{Na}_{0.3}\text{CoO}_2 \cdot 1.3\text{H}_2\text{O}$  by  $^{59}\text{Co}$  and  $^{17}\text{O}$  Nuclear Magnetic Resonance (NMR). For  $\text{Na}_{0.72}\text{CoO}_2$ ,  $^{59}\text{Co}$  NMR line shape shows clearly that there are two types of Co sites – Co(A) site and Co(B) site. The electronic character of Co(A) site is close to that of the less magnetic  $\text{Co}^{+3}$ -like ion with spin  $\sim 0$ , while the electronic character of Co(B) site is close to that of the strongly magnetic  $\text{Co}^{+4}$ -like ions with spin  $\sim \frac{1}{2}$ . The temperature dependence of the Knight shifts suggests that the Co(A) and Co(B) sites are electronically coupled, which is not consistent with simple phase separation. The local Co electronic environments propagate to the adjacent O layers through p-d hybridization. Therefore, there are two types of oxygen sites, O(A) site and O(B) site. We introduced a different route to do  $K$  vs  $\chi$  plot analysis for the Co sites and determined that for the Co sites,  $K_{\text{orbital}}(\text{A})$  is 1.816 % and  $K_{\text{spin}}(\text{A})$  is about  $\sim 0.2$  %;  $K_{\text{orbital}}(\text{B})$  is 4.0255 % and  $K_{\text{spin}}(\text{B})$  is at least 1.5 %. For  $\text{Na}_{0.3}\text{CoO}_2$ ,  $^{59}\text{Co}$  NMR line shape shows that the Co valence is averaged out in this material. There are two types of oxygen sites, O(C) site and O(D) site, presumably because of the nearest neighbor  $\text{Na}^+$  sites. The constant behavior of Knight shifts below 100 K for both the Co and O sites suggests the emergence of a low temperature canonical Fermi-liquid behavior. For the superconductor  $\text{Na}_{0.3}\text{CoO}_2 \cdot 1.3\text{H}_2\text{O}$ , both  $^{59}\text{Co}$  and  $^{17}\text{O}$  NMR line shapes show that there is only one type of Co site and oxygen site. The Knight shifts of  $^{59}\text{Co}$  and  $^{17}\text{O}$  are temperature independent below 100 K down to  $T_c$ . Combined with our spin-lattice relaxation  $1/T_1T$  measurements, we can rule out the possibility of ferromagnetic scenario of spin excitations above  $T_c$ .

# Acknowledgements

I would like to give my first thanks to my supervisor, Dr. Takashi Imai, for his guidance, support in the past two years. I am very grateful for his consideration and many helps since I came to Canada as an international student. In academic, his suggestions and advices were always crucial to continue and finish this research project. His knowledge and high academic standard could always make our experiment results published and recognized by other scientists.

I also want to thank Dr. An-Chang Shi and Dr. Graeme Luke who are in my supervisory committee, for their time and suggestions. Many thanks to people who are working or worked in our group, Shanta Ranjan Saha, Sarah Golin, Matthew Van Dyken, for their collaborations. I also appreciate many helps from Dr. Paul Dube, who can always provide us enough helium for experiments.

Many thanks to the people working in the general office, Daphne Kilgour, Mara Esposto, Cheryl Johnston, who helped me so many times for all kinds of things. Their helps made my life in Canada easier.

A lot of friends I met in Physics department, Zhang Rui, Zhou Zhuowei, Zhao Yang, Zhou Jiajia, Yang Jing, Lin Fei, Chen Jun, Jose Rodriguez, Greg MacDougall, Jungseek Hwang, Sung-Jae Kim etc. helped me a lot and made my abroad life more colorful, thank you, guys! All in all, I was so lucky to work with and be friends with such a great group people in McMaster.

Last but not least, I would like to thank my wife and all my other family members for their love, encouragement, concern and support to me all along.

*Hamilton, Ontario*

*December, 2005*

Fanlong Ning

# Contents

Abstract	iii
Acknowledgements	iv
Table of Contents	v
List of Figures	vii
List of Tables	xi
<b>1 INTRODUCTION</b>	<b>1</b>
1.1 New Superconductor — $\text{Na}_{0.3}\text{CoO}_2\text{-}1.3\text{H}_2\text{O}$	1
1.2 Crystal Structure of $\text{Na}_x\text{CoO}_2\text{-}y\text{H}_2\text{O}$	2
1.3 Transport and Magnetic Properties	4
1.4 Organization of Thesis	7
<b>2 EXPERIMENTAL TECHNIQUE</b>	<b>8</b>
2.1 Sample Preparation and Characterization	8
2.1.1 Sample Preparation	8
2.1.2 Sample Characterization by X-ray and SQUID	9
2.2 Introduction of Nuclear Magnetic Resonance	12

2.2.1	NMR/NQR Frequency and Knight Shift . . . . .	12
2.2.2	Nuclear Quadrupole Interaction . . . . .	14
2.2.3	Electronics . . . . .	17
2.2.4	NMR Summary . . . . .	22
<b>3</b>	<b>COBALT AND OXYGEN NMR RESULTS AND ANALYSIS</b>	<b>23</b>
3.1	Contributions of NMR Community . . . . .	23
3.2	Results and Analysis of $\text{Na}_{0.72}\text{CoO}_2$ . . . . .	24
3.2.1	$^{59}\text{Co}$ and $^{17}\text{O}$ NMR line shapes . . . . .	24
3.2.2	Knight Shift . . . . .	28
3.2.3	The $K \sim \chi$ Plot . . . . .	31
3.3	Results and Analysis of $\text{Na}_{0.3}\text{CoO}_2$ . . . . .	37
3.3.1	Line shapes and Knight Shift . . . . .	37
3.3.2	The $K \sim \chi$ Plot . . . . .	43
3.4	Results and Analysis of $\text{Na}_{0.3}\text{CoO}_2 \cdot 1.3\text{H}_2\text{O}$ . . . . .	43
3.4.1	Line shapes and Knight Shift . . . . .	43
<b>4</b>	<b>CONCLUSION</b>	<b>51</b>
	<b>References</b>	<b>53</b>
	<b>Appendix</b>	<b>56</b>

# List of Figures

1.1	Perspective of $P6_3/mmc$ structure of $\text{Na}_x\text{CoO}_2$ (left panel) and $\text{Na}_x\text{CoO}_2 \cdot y\text{H}_2\text{O}$ (right panel). . . . .	3
1.2	The susceptibility $\chi$ under 5 Tesla field applied within ab-plane is shown in panel (A). The in-plane resistivity $\rho$ is shown in panel (B). The c-axis lattice constant versus Na concentration $x$ determined by ICP is plotted in panel (C). . . . .	5
1.3	The phase diagram of nonhydrated $\text{Na}_x\text{CoO}_2$ provided by Foo et al. The charge-ordered insulating state at $\frac{1}{2}$ is sandwiched between the paramagnetic metal at 0.3 and the Curie -Weiss metallic state at 0.65 – 0.75. The superconducting state is obtained on intercalation with $\text{H}_2\text{O}$ . . . . .	6
2.1	Main panel: Powder X-ray diffraction patterns (Cu $K\alpha$ radiation) of $\text{Na}_{0.3}\text{CoO}_2 \cdot 0.6\text{H}_2\text{O}$ . Inset: an enlargement of the 002 reflections for each sample, highlighting the shift in the layer spacing as a function of sodium content . . . . .	10

2.2	Upper panel: Magnetic susceptibility of ceramic $\text{Na}_{0.72}\text{CoO}_2$ with an applied field of 1 Tesla, solid line is Curie-Weiss fit. Lower panel: Magnetic susceptibility of $\text{Na}_{0.3}\text{CoO}_2\cdot 1.3\text{H}_2\text{O}$ with an applied field of 20 Oe, the diamagnetic values above $T_c$ arise from water mixed with the sample. The Curie tail above $T_c$ and below 30 K is from magnetic impurities, not intrinsic property of the sample (see NMR data later in this thesis). Inset: The DC susceptibility measured under FC and ZFC conditions in an applied field of 20 Oe. . . . .	11
2.3	(a) Energy levels for NMR with spin $I = \frac{3}{2}$ nucleus. (b) NMR resonance spectra for spin $I = \frac{3}{2}$ . . . . .	18
2.4	Schematic of electronics for NMR spectrometer, Imai labs. . . . .	20
3.1	$^{59}\text{Co}$ NMR line shape of aligned ceramics $\text{Na}_{0.72}\text{CoO}_2$ at 200 K with $H_{ext}$ applied within the ab plane. The arrows indicate the central transition $\nu_{-\frac{1}{2}, \frac{1}{2}}$ at two different sites. Some of the furthest satellite transitions are not shown above 88 MHz because $^{23}\text{Na}$ NMR line was superposed. . . . .	25
3.2	$^{17}\text{O}$ NMR line shape of aligned ceramics $\text{Na}_{0.72}\text{Co}^{17}\text{O}_2$ at 77 K with $H_{ext}$ applied within the ab plane. We applied an inversion pulse and waited for 2 msec before recording the spin echo intensity to separate the O(B) site with "fast" relaxation times. By taking the difference between the whole echo intensity ("slow") and the fast O(B) contributions ( $-\circ-$ ), we deduced the line shape of O(A) site("difference" $-\diamond-$ ) . . . . .	27

3.3	Upper panel: $^{59}\text{Co}$ NMR Knight shift for Co(A) site ( $\blacklozenge$ ) and Co(B) site ( $\bullet$ ) with $H_{ext}$ applied along ab-plane, solid lines are Curie-Weiss fit $^{59}\text{K(A)} = 2.0884 + \frac{34.8}{T+27}$ (%) and $^{59}\text{K(B)} = 5.335 + \frac{224.5}{T+28.6}$ (%). Lower panel: The Knight shift of Co(B) versus that of Co(A), the solid line is linear fit with a slope = 6.2. . . . .	29
3.4	Upper panel: $^{17}\text{O}$ NMR Knight shift for O(A) site ( $\diamond$ ) and O(B) site ( $\circ$ ) with $H_{ext}$ applied along ab-plane, solid lines are Curie-Weiss fit $^{17}\text{K(A)} = 0.02418 + \frac{4.3}{T+29.8}$ (%) and $^{17}\text{K(B)} = 0.1298 + \frac{36.4}{T+27.3}$ (%). Lower panel: The Knight shift of O(B) versus that of O(A), the solid line is linear fit with a slope = 9.1. . . . .	30
3.5	$^{59}\text{Co}$ Knight shift versus bulk magnetic susceptibility $\chi$ plot of $\text{Na}_{0.72}\text{CoO}_2$ . Notice that point A and B should have same x-axis coordinate. . . . .	33
3.6	Main panel: $^{59}\text{Co}$ line shape of single crystal $\text{Na}_{0.3}\text{CoO}_2$ at 4.2 K with $H_{ext}$ applied parallel to the c-axis. $\nu_c \sim 4$ MHz. Inset: $^{59}\text{Co}$ NMR Knight shift of single crystal $\text{Na}_{0.3}\text{CoO}_2$ with $H_{ext}$ applied parallel to the c-axis. . . . .	38
3.7	$^{17}\text{O}$ line shapes of aligned ceramics $\text{Na}_{0.35}\text{CoO}_2$ with $H_{ext}$ applied within the ab plane. O(C) site (filled arrows) merge with O(D) site (open arrows) to a single line with temperature increasing. . . . .	39
3.8	$^{17}\text{O}$ NMR Knight shift for O(C) site ( $\square$ ) and O(D) site ( $\triangle$ ) with $H_{ext}$ applied along ab-plane. The Knight shifts of both sites are same at 295 K due to motion narrowing effect. . . . .	40
3.9	$^{59}\text{Co}$ Knight shift with $H_{ext}$ along c-axis versus bulk magnetic susceptibility $\chi$ plot of $\text{Na}_{0.35}\text{CoO}_2$ . . . . .	42
3.10	$^{59}\text{Co}$ NMR line shape of single crystal $\text{Na}_{0.3}\text{CoO}_2\text{-}1.3\text{H}_2\text{O}$ at 77 K with $H_{ext}$ applied within the ab plane. $\nu_{ab} \sim 1.85$ MHz. . . . .	45

3.11	The powder pattern $^{17}\text{O}$ NMR line shapes of $\text{Na}_{0.35}\text{CoO}_2-1.3\text{H}_2\text{O}$ ceramics at 77 K. The less pronounced peak structures and the high and low frequency tails are due to random orientations of the sample. . .	46
3.12	$^{59}\text{Co}$ NMR Knight shift( $\blacktriangledown$ ) of single crystal $\text{Na}_{0.3}\text{CoO}_2-1.3\text{H}_2\text{O}$ with $H_{ext}$ applied parallel to the ab-plane and $^{17}\text{O}$ NMR Knight shift( $\nabla$ ) of unaligned ceramics $\text{Na}_{0.3}\text{Co}^{17}\text{O}_2-1.3\text{H}_2\text{O}$ . . . . .	47
3.13	$^{59}\text{Co}$ Knight shift with $H_{ext}$ along ab plane versus bulk magnetic susceptibility $\chi$ plot of $\text{Na}_{0.3}\text{Co}^{17}\text{O}_2-1.3\text{H}_2\text{O}$ . . . . .	49
3.14	$^{17}\text{O}$ Knight shift with $H_{ext}$ along ab plane versus bulk magnetic susceptibility $\chi$ plot of $\text{Na}_{0.3}\text{Co}^{17}\text{O}_2-1.3\text{H}_2\text{O}$ . . . . .	50

# List of Tables

3.1	Values from $K \sim \chi$ plot for Co sites of $\text{Na}_{0.72}\text{CoO}_2$ . . . . .	36
-----	---	----

# Chapter 1

## INTRODUCTION

### 1.1 New Superconductor — $\text{Na}_{0.3}\text{CoO}_2\text{-}1.3\text{H}_2\text{O}$

Research on the mechanism of high- $T_c$  Superconductivity remains an important topic in condensed matter physics nearly 20 years after the initial discovery of high- $T_c$  copper oxide superconductor (abbr. cuprates)  $\text{La}_{2-x}\text{Ba}_x\text{CuO}_4$  in 1986 (Bednorz and Müller, 1986). Most cuprates show a very high transition temperature compared with conventional metal or alloy superconductors which can be well described by the Bardeen-Cooper-Schrieffer (BCS) theory (Bardeen et al., 1957). Over the past 19 years, scientists have made considerable progress in understanding the mechanism and concluded that strongly correlation effects of electrons in the  $\text{CuO}_2$  planes are crucial for superconductivity. However, existing theoretical models can't satisfactorily explain the mechanism yet. Persistent effort is still underway to further understanding in both theory and experiment. One emerging line of research is to search for new oxide superconductors, which may share some common features with the cuprates, and hence provide valuable clues. A newly discovered superconductor,  $\text{Na}_{0.3}\text{CoO}_2\text{-}1.3\text{H}_2\text{O}$ , with  $T_c = 4.5$  K is one of those promising materials (Takada et al., 2003).

The non-hydrated parent compound  $\text{Na}_x\text{CoO}_2$  with  $x \sim 0.5$  had been studied earlier due to its unconventionally large thermoelectric power (Terasaki et al., 1997), and research on such anomalous behavior boomed after the discovery of superconductivity in the hydrated  $\text{Na}_{0.3}\text{CoO}_2 \cdot 1.3\text{H}_2\text{O}$ . This discovery is quite exciting, because the  $\text{CoO}_2$  layers form a triangular lattice. Moreover, one can view the  $\text{CoO}_2$  layers as carrier doped spin  $S = 1/2$  triangular lattice. We recall that the high- $T_c$  cuprates have carrier doped  $\text{CuO}_2$  planes with  $S = 1/2$   $\text{Cu}^{+2}$  ions. This suggests that research into  $\text{Na}_{0.3}\text{CoO}_2 \cdot 1.3\text{H}_2\text{O}$  may shed new light on the mechanism of the unconventional High- $T_c$  superconductivity. Another interesting aspect is that P.W.Anderson has suggested (Anderson, 1987) that frustration of spins may be related to high- $T_c$  superconductivity (i.e. RVB theory).  $\text{Na}_x\text{CoO}_2$  is an ideal material to investigate the possibility of RVB superconductivity because frustration effects could be very strong in the triangular lattice if spin-spin exchange interaction is predominantly anti-ferromagnetic.

## 1.2 Crystal Structure of $\text{Na}_x\text{CoO}_2 \cdot y\text{H}_2\text{O}$

The structure of the  $\text{Na}_x\text{CoO}_2 \cdot y\text{H}_2\text{O}$  is of the  $P6_3/mmc$  space group, as shown in Figure 1.1 (Jorgensen et al., 2003). The Co ions form a triangular lattice. Each Co is located in the center of the oxygen octahedra. The unit cell is built up by two sheets of edge-sharing  $\text{CoO}_6$  octahedra, which are rotated by  $60^\circ$  with respect to each other. Na ions form charge reservoir layers in between and separate the  $\text{CoO}_2$  layers to make this material quasi-two dimensional. The Na concentration can vary from  $x \sim 0.25$  to 1. It is widely speculated that vacancies of Na ions are spatially ordered for some  $x$  values. For  $\text{Na}_x\text{CoO}_2$  ( $x = 0.72, 0.3$ ), structure studies by Neutron scattering (Huang et al., 2004a,b) show that the Na ions have two possible positions, Na(1):  $2b(0\ 0\ 1/4)$  and Na(2):  $2c(2/3\ 1/3\ 1/4)$ . The Na ions are surrounded by six oxygen ions

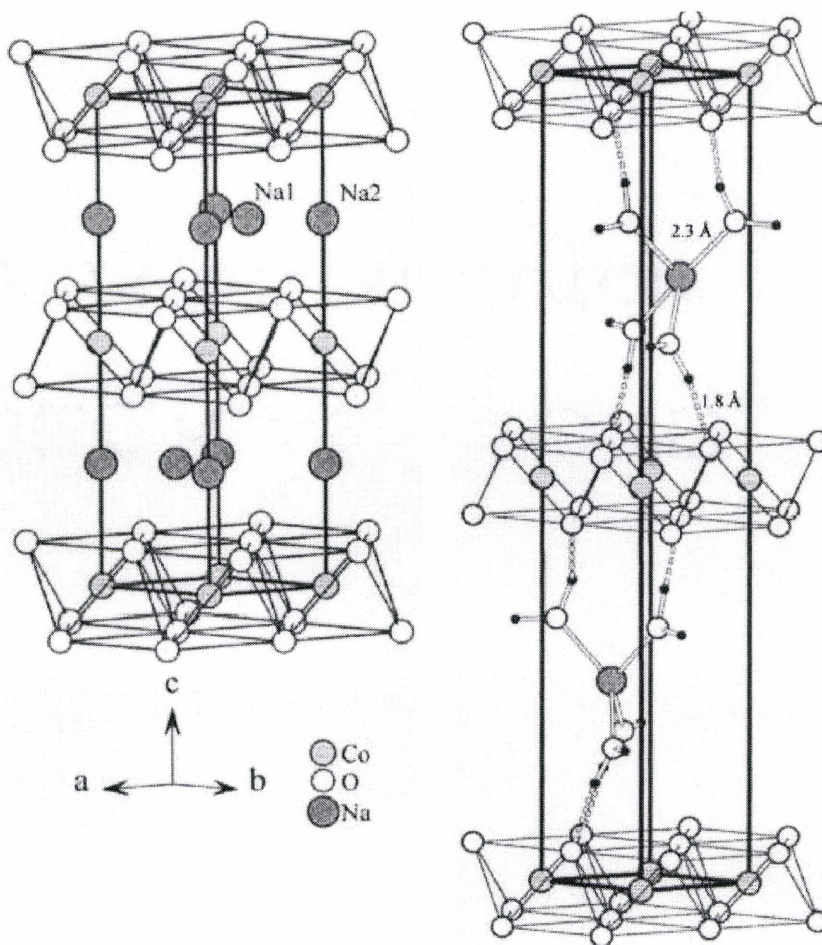


Figure 1.1 Perspective of  $P6_3/mmc$  structure of  $\text{Na}_x\text{CoO}_2$  (left panel) and  $\text{Na}_x\text{CoO}_2-y\text{H}_2\text{O}$  (right panel).

to form a triangular polyhedron. The Na(1)O<sub>6</sub> triangular polyhedron is face sharing with two CoO<sub>6</sub> octahedra (directly above and below) and the Na(2)O<sub>6</sub> triangular polyhedron is corner sharing with six CoO<sub>6</sub> octahedra in the nearest CoO<sub>2</sub> blocks. For the superconducting Na<sub>0.3</sub>CoO<sub>2</sub>-1.3H<sub>2</sub>O, water molecules form two additional layers between the Na and CoO<sub>2</sub> layers. The water molecules form a structure that replicates the structure of ice (Jorgensen et al., 2003). It has been firmly established that the water molecules lengthen the c-axis lattice parameter. However, whether the Na(2) ions occupy  $2d(1/3 \ 2/3 \ 1/4)$  or  $2c(2/3 \ 1/3 \ 1/4)$  is still controversial for the superconductor Na<sub>0.3</sub>CoO<sub>2</sub>-1.3H<sub>2</sub>O (Lynn et al., 2003). In addition, suggestions have been made that H<sub>2</sub>O molecules are charged in the superconductors, i.e. H<sub>2</sub>O may be doping electrons into CoO<sub>2</sub> layers (Milne et al., 2004, Takada et al., 2004).

### 1.3 Transport and Magnetic Properties

With the Na concentration  $x$  increasing from 0.3 to 0.82, the ground state of the Na <sub>$x$</sub> CoO<sub>2</sub> compound varies from a paramagnetic metal ( $x = 0.3$ ) to a charge-ordered insulator (at  $x = 0.5$ ), then to a Curie-Weiss metal (at  $x > 0.7$ ) (Foo et al., 2004).

For samples with  $0.72 < x < 0.78$ , three phase transitions have been observed at  $T_c = 22$  K,  $T_k = 9$  K, and  $T_2 \sim 340$  K (Sakurai et al., 2004a,b). The first two are second order phase transitions which can be identified in the magnetic susceptibility and specific heat, and both are independent of the concentration  $x$ . The transition at 22 K is believed to be due to spin density wave formation (Motohashi et al., 2003), while the one at 9 K is probably caused by a weakly ferromagnetic transition. Both transitions disappear for materials with  $x < 0.72$ . Resistance measurements show that there is a kink around 340 K, indicating a first order phase transition from Na

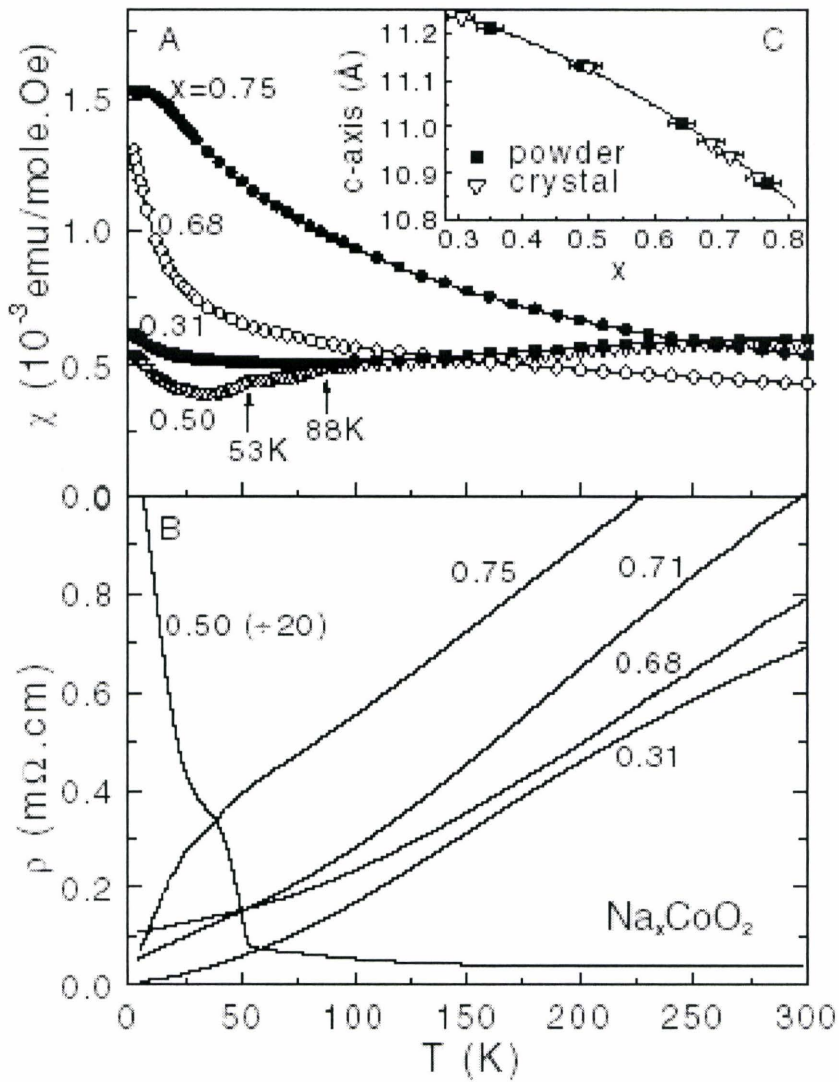


Figure 1.2 The susceptibility  $\chi$  under 5 Tesla field applied within ab-plane is shown in panel (A). The in-plane resistivity  $\rho$  is shown in panel (B). The c-axis lattice constant versus Na concentration  $x$  determined by ICP is plotted in panel (C).

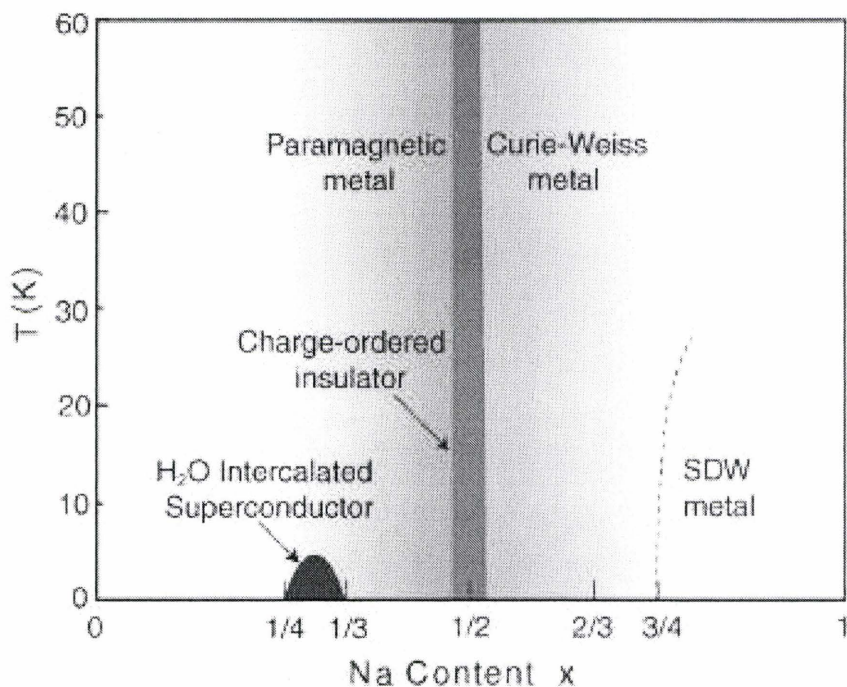


Figure 1.3 The phase diagram of nonhydrated  $\text{Na}_x\text{CoO}_2$  provided by Foo et al. The charge-ordered insulating state at  $\frac{1}{2}$  is sandwiched between the paramagnetic metal at 0.3 and the Curie-Weiss metallic state at 0.65 – 0.75. The superconducting state is obtained on intercalation with  $\text{H}_2\text{O}$ .

ordering with a latent heat about 700 J/mol (Sales et al., 2004).

For  $x = 0.3$ , the resistivity follows a  $\rho \sim T^2$  behavior below 100 K, which is evidence for a canonical Fermi-liquid state. Figure 1.2 and Figure 1.3 show some representative data and the phase diagram proposed by Foo et al (Foo et al., 2004).

## 1.4 Organization of Thesis

Massive studies on this material have just started around the world and we are still far from a clear understanding of the properties of  $\text{Na}_x\text{CoO}_2$ . The results presented in this thesis are a part of the massive research work over the last several years. Our primary focus will be on Nuclear Magnetic Resonance (NMR) measurements conducted by us in the past 2 years. The thesis includes three additional chapters: Chapter 2 presents a brief introduction to experimental method and theoretical background of the NMR. Chapter 3 shows the experimental results of NMR line shapes and Knight shifts for  $\text{Na}_x\text{CoO}_2$  ( $x = 0.72, 0.3$ ) and superconductor  $\text{Na}_{0.3}\text{CoO}_2 \cdot 1.3\text{H}_2\text{O}$ , and the analysis of Knight shift based on  $K \sim \chi$  plot. Conclusions derived from the current work are given in Chapter 4.

# Chapter 2

## EXPERIMENTAL TECHNIQUE

### 2.1 Sample Preparation and Characterization

#### 2.1.1 Sample Preparation

The single phase, polycrystalline samples  $\text{Na}_{0.72}\text{CoO}_2$  used in this study were prepared using conventional solid state reactions. We mixed the predried materials  $\text{Co}_3\text{O}_4$  (99.9985%) and  $\text{Na}_2\text{CoO}_3$  (99.997%) with appropriate nominal ratio, and then ground the mixture for about 1 hour in an agate mortar to obtain very fine and well-mixed powder. We pressed the pellet under 2.6 Kbar, preheated it at 750 °C for 12 hours, followed by re-grinding and reheating the pellet 3 times at 850 °C in flowing  $\text{O}_2$  gas. We heated sample by fast-heating method (Motohashi et al., 2001) in all steps to minimize Na loss except the last step in which the pellet was cooled down within a furnace in order to ensure uniform oxygen content. This slow furnace cooling procedure should also provide the Na ions with enough time to find their equilibrium positions in the crystal. Based on  $^{23}\text{Na}$  NMR measurements by us and other groups (Gavilano et al., 2004), it is known that Na motion can be activated at as low as  $\sim 50$

°C hence low temperature annealing could potentially affect the physical properties.

$\text{Na}_{0.3}\text{CoO}_2$  was prepared by stirring 0.5 g  $\text{Na}_{0.72}\text{CoO}_2$  in 20 ml 6 M bromine and acetonitrile solutions to deintercalate sodium for 5 days. The product was washed several times with acetonitrile and then water. Subsequently, we dried it at 200 °C to get single phase polycrystal  $\text{Na}_{0.3}\text{CoO}_2$  without undesired water intercalation. To obtain superconducting  $\text{Na}_{0.3}\text{CoO}_2\cdot 1.3\text{H}_2\text{O}$ , we soaked  $\text{Na}_{0.3}\text{CoO}_2$  into purified water for typically 5 to 10 days. To conduct  $^{17}\text{O}$  NMR measurement (natural abundance 0.037%), we need to enrich the sample with  $^{17}\text{O}$  isotope. We annealed  $\text{Na}_{0.72}\text{CoO}_2$  in 50%  $^{17}\text{O}_2$  isotope in a sealed quartz tube at 800 °C for 5 days to get  $\text{Na}_{0.72}\text{Co}^{17}\text{O}_2$ . Then repeated above procedures to get  $\text{Na}_{0.3}\text{Co}^{17}\text{O}_2$  and superconductor  $\text{Na}_{0.3}\text{Co}^{17}\text{O}_2\cdot 1.3\text{H}_2\text{O}$ . All the good dry samples are black and a little shiny, typical of metallic correlated-electron oxides.

### 2.1.2 Sample Characterization by X-ray and SQUID

We characterized our samples by powder X-ray diffraction, and confirmed that all of our samples used in this study are single phase. We present some X-ray patterns in Figure 2.1. Earlier report by Foo et al (Foo et al., 2004) demonstrated that the Na concentration has a monotonous relation with the c-axis lattice constant. This means that we can estimate Na concentration of our samples based on the latter. The sodium concentration in the samples are confirmed to be 0.72 and 0.3, respectively, with uncertainties  $\pm 0.04$  estimated from the width of the (002) X-ray diffraction peak.

We measured the magnetic susceptibility of all samples by SQUID. We can fit the data of  $\text{Na}_{0.72}\text{CoO}_2$  by Curie-Weiss law with a negative Weiss temperature  $\theta = 27$  K, this is consistent with earlier results (Foo et al., 2004). For  $\text{Na}_{0.3}\text{CoO}_2$  and

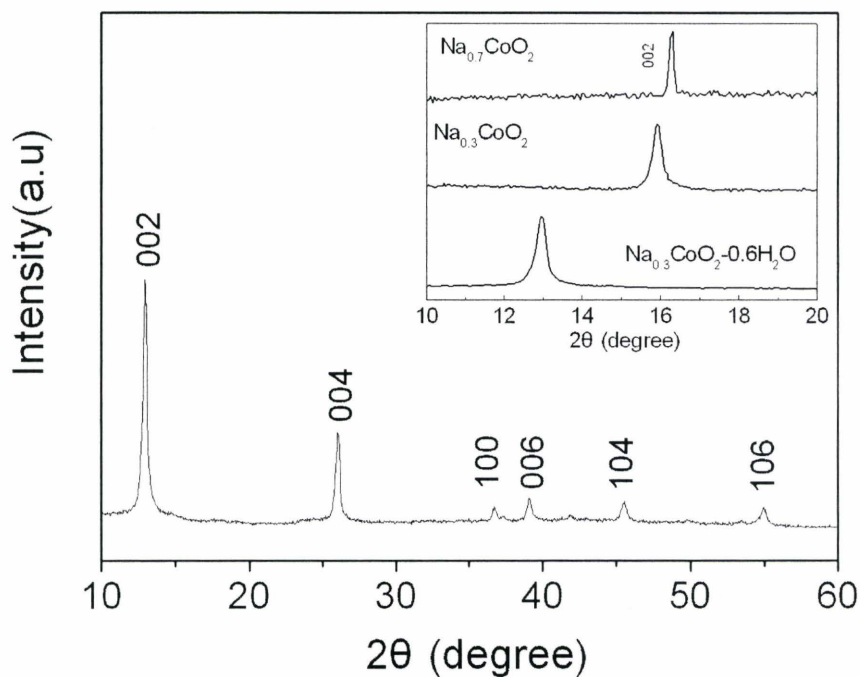


Figure 2.1 Main panel: Powder X-ray diffraction patterns ( $\text{Cu K}\alpha$  radiation) of  $\text{Na}_{0.3}\text{CoO}_2-0.6\text{H}_2\text{O}$ . Inset: an enlargement of the 002 reflections for each sample, highlighting the shift in the layer spacing as a function of sodium content

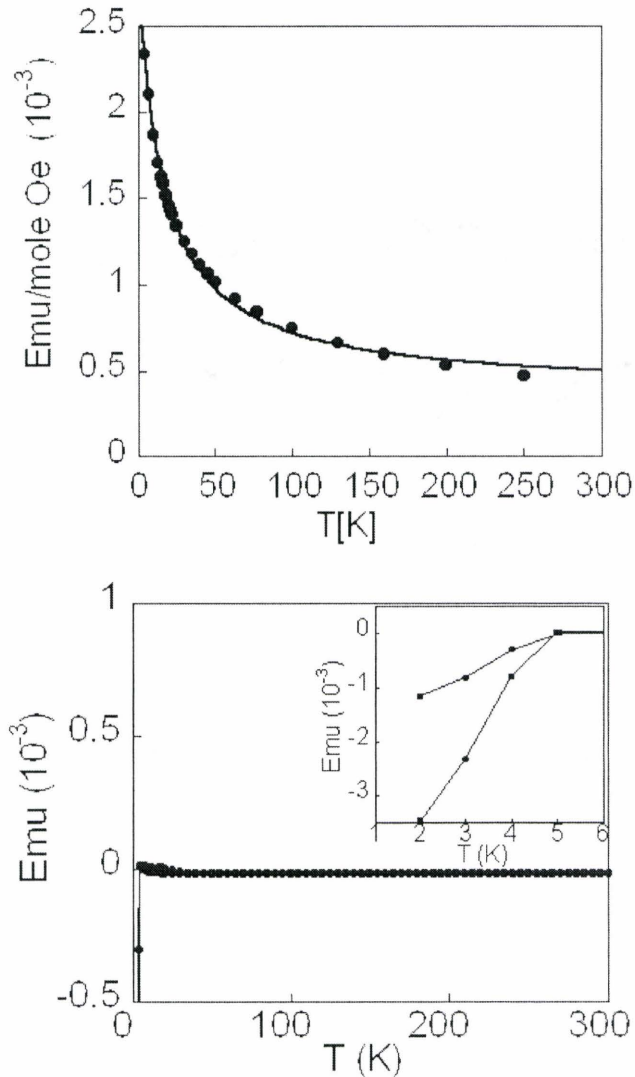


Figure 2.2 Upper panel: Magnetic susceptibility of ceramic  $\text{Na}_{0.72}\text{CoO}_2$  with an applied field of 1 Tesla, solid line is Curie-Weiss fit. Lower panel: Magnetic susceptibility of  $\text{Na}_{0.3}\text{CoO}_2-1.3\text{H}_2\text{O}$  with an applied field of 20 Oe, the diamagnetic values above  $T_c$  arise from water mixed with the sample. The Curie tail above  $T_c$  and below 30 K is from magnetic impurities, not intrinsic property of the sample (see NMR data later in this thesis). Inset: The DC susceptibility measured under FC and ZFC conditions in an applied field of 20 Oe.

$\text{Na}_{0.3}\text{CoO}_2\cdot 1.3\text{H}_2\text{O}$ , most samples show a Curie tail at low temperatures. The origin of such a Curie tail was quite controversial until we demonstrated unambiguously by  $^{17}\text{O}$  and  $^{59}\text{Co}$  NMR that it is not due to ferromagnetic correlations but due to magnetic defects or impurities (Ning et al., 2004, Ning and Imai, 2005). After subtracting these impurity contributions, we found that  $\chi$  is independent of temperature below  $\sim 100$  K. For  $\text{Na}_{0.3}\text{CoO}_2\cdot 1.3\text{H}_2\text{O}$ , as shown in Figure 2.2, the strong diamagnetic signals provide evidence for bulk superconductivity below 4.5K. Unfortunately, we couldn't separate the contributions from the superconductor and the water(if we dry the sample, we will lose superconductivity).  $\chi$  is negative even above  $T_c$ . This is due to the diamagnetic contributions from pure water.

## 2.2 Introduction of Nuclear Magnetic Resonance

### 2.2.1 NMR/NQR Frequency and Knight Shift

The magnetic moment  $\mu$  associated with electron or nuclear spins interacts with a static magnetic field  $H$ . This interaction energy can be expressed by a simple Hamiltonian:

$$H = -\vec{\mu} \cdot \vec{H} = -\gamma\hbar H_0 I_z \quad (2.1)$$

where we assume that the magnetic field is along the z-direction.  $\gamma$  is a scalar called the *nuclear gyromagnetic ratio* which is a constant known from other experiments.  $I_z$  is the angular momentum operator along the z-direction. The energy level will split, by Zeeman effect. For nuclear spin  $I$  with spin  $I = 3/2$ , the  $2I$  transitions between these energy levels all have the same energy  $E$ . If at this time, we apply an alternating magnetic field  $H_1$  with frequency  $\omega_n$  perpendicular to the z-axis, the resonance will occur if  $\hbar\omega_n = \gamma_n H_0$  is satisfied, where  $\gamma_n$  is the nuclear gyromagnetic ratio of the

nuclei.

However, in addition to an external magnetic field  $H_0$ , the surrounding electrons will induce additional magnetic field  $\Delta H$  on the nuclei by hyperfine interaction between nuclear spin  $I$  and electrons, so the total field exerted on the nuclei will be the applied field  $H$  plus the additional field  $\Delta H$ . Then the resonance frequency  $\omega_n$  is

$$\hbar\omega_n = \gamma(H_0 + \Delta H) = \gamma H_0 \left(1 + \frac{\Delta H}{H_0}\right) = \gamma H_0(1 + K) \quad (2.2)$$

where  $K$  is the famous Knight shift which is essentially the fractional frequency shift. Knight shift from NMR measurements provides very important information. It measures the magnetic susceptibility of the material at the position of the nucleus in response to the uniform applied field.

The contributions to the uniform magnetic susceptibility can be separated into three parts: the electron spin susceptibility,  $\chi_{spin}(q = 0)$  where  $q$  is wave number; the electron orbital susceptibility (Van Vleck)  $\chi_{orbital}$ ; and the diamagnetic susceptibility  $\chi_{dia}$  (Ashcroft and Mermin, 1976). The diamagnetic susceptibility is a quantum mechanical effect that arises from the the diamagnetic shielding current of the electrons, and does not have any temperature dependence. The orbital susceptibility arises from the mixing of the atomic energy levels in the presence of the magnetic field. In a particular crystal structure, the atomic energy levels are split by the crystal field. In the presence of a perturbing magnetic field, these atomic levels are no longer eigenstates and a small amount of mixing of these atomic orbitals occurs (Ashcroft and Mermin, 1976). The important fact is that because the energy separation between the atomic orbitals caused by the crystal field is about  $1 \text{ eV} = 11,600 \text{ K}$ , compared with the temperature range for general NMR experiments ( $\sim 300 \text{ K}$ ), the orbital susceptibility generally will not have significant temperature dependence. We can consider this term

as temperature independent in our calculations. Thus, the only part of the susceptibility with a temperature dependence is the electron spin susceptibility  $\chi_{spin}(q = 0)$ . We may express Knight shift as (Jaccarino, 1966)

$$K = \frac{A(q = 0)}{N_A \mu_B} \chi_{spin}(q = 0) + K_{orbital} + K_{dia} \quad (2.3)$$

where  $K_{orbital}$  and  $K_{dia}$  are the Knight shift arising from the orbital and diamagnetic susceptibility, respectively.  $A(q = 0)$  is the *hyperfine coupling* between the electron spin and the nuclear spin with wave vector  $q = 0$  and  $N_A$  is the Avogadro's constant number. We can express eq(2.3) as:

$$A(q = 0) = N_A \mu_B \frac{\Delta K}{\Delta \chi_{spin}(q = 0)} \quad (2.4)$$

If we plot Knight shift as a function of bulk uniform susceptibility  $\chi$  with temperature as an implicit parameter (abbr.  $K \sim \chi$  plot), the slope is proportional to the hyperfine coupling  $A(q = 0)$ . The hyperfine coupling between the electron spin and the nuclei spin quantifies how much interaction energy between the spins is, or alternatively, how much magnetic field is produced at the location of the nucleus by an electron spin. Based on the  $K \sim \chi$  plot and further calculations, we can separate all three contributions for both bulk susceptibility and Knight shift. Detailed of the method will be shown in the forthcoming chapters.

## 2.2.2 Nuclear Quadrupole Interaction

In addition to the magnetic interaction between the nucleus and a magnetic fields (for  $I \neq 0$ ), the nucleus with  $I \geq 1$  will also interact with the charge environment via nuclear quadrupole interaction. To understand this interaction, we expand the

nuclear charge distribution in spherical harmonics of order  $l$ . The nucleus does have a monopole moment ( $l = 0$ , its charge  $Ze$ ) which will interact with an electric field. However, this interaction is independent of the direction of the spin of the nucleus, so it does not affect the transitions between energy levels which are of interest here. Next moment is the electric dipole moment ( $l = 1$ ), which is prohibited by the fact that nuclear states have well-defined parity. In fact parity prohibits any charge multipoles with odd  $l$ .

The quadrupole moment ( $l = 2$ ),  $Q$ , is defined by the expression (Kittel, 1996)

$$Q = \frac{1}{2e} \int (3z^2 - r^2) \rho(\vec{r}) d^3x \quad (2.5)$$

where  $\rho(\vec{r})$  is the charge distribution of the nucleus for the  $I_z = I$  state and  $e = |e|$  is the electron charge. Since the unit of  $\rho(\vec{r})$  is that of charge divided by volume, the quadrupole moment  $Q$  has units of area. If  $\rho(\vec{r})$  is only a function of  $|\vec{r}|$  (spherically symmetric) then the quadrupole moment disappears. If the charge distribution is extended along the  $z$  axis, the quadrupole moment will be positive. While if  $\rho(\vec{r})$  is flattened in the  $xy$  plane, the quadrupole moment will be negative.

High order moments of the charge distribution do exist, but the interaction effects are expected to be very small. The interaction strength is expected to fall off as (Abragam, 1961, Slichter, 1990)

$$\left(\frac{R_n}{R_e}\right)^l \approx (10^{-5})^l \quad (2.6)$$

where  $R_n$  and  $R_e$  represent the radius of the nuclear and electronic charge distributions, respectively. The rapid fall off of the interaction strength with increasing  $l$  is already seen between  $l = 0$  and  $l = 2$ . The  $l = 0$  interaction energy is of the order of 10 eV. On the other hand, typical quadrupole resonant frequencies are on the order

of 10 MHz  $\sim 10^{-8}$  eV, which is about 10 orders of magnitude weaker.

The quadrupole moment of the nucleus interacts with the electric field gradient at the position of the nucleus, and probes the local charge environment. The quadrupole Hamiltonian is (Abraham, 1961, Slichter, 1990)

$$H = \frac{\nu_Q \hbar}{2} [I_z^2 - \frac{1}{3} I(I+1) + \frac{1}{6} \eta (I_+^2 + I_-^2)], \quad (2.7)$$

where  $I$  is the spin of the nucleus ( $I = \frac{7}{2}$  for  $^{59}\text{Co}$  and  $I = \frac{5}{2}$  for  $^{17}\text{O}$ ). The  $z$  component of the quadrupole coupling  $\nu_Q$  is given by

$$\nu_Q^z = \frac{3e^2 q_z}{2hI(I+1)} Q, \quad (2.8)$$

where  $Q$  is the quadrupole moment of the nucleus as defined above and  $eq_z$  is the  $z$  axis component of the electric field gradient at the nuclear position. Writing the electrostatic potential as  $V$ , we have  $eq_z = \frac{\partial^2 V}{\partial z^2}$ . The Laplace equation for the electrostatic potential is,

$$\frac{\partial^2 V}{\partial x^2} + \frac{\partial^2 V}{\partial y^2} + \frac{\partial^2 V}{\partial z^2} = 0. \quad (2.9)$$

This implies that the three principle components of the quadrupole interaction will also sum to zero,

$$\nu_Q^x + \nu_Q^y + \nu_Q^z = 0. \quad (2.10)$$

The electric field gradient is axially symmetric and  $\nu_Q^x = \nu_Q^y = -\nu_Q^z/2$  if the local symmetry is cubic or tetragonal. More generally,  $\nu_Q^x \neq \nu_Q^y$ , and the asymmetry of the electric field gradient is given by  $\eta$ , define as,

$$\eta = \left| \frac{\nu_Q^x - \nu_Q^y}{\nu_Q^z} \right| \quad (2.11)$$

where we take  $|\nu_Q^z| \geq |\nu_Q^y| \geq |\nu_Q^x|$  by our choice of the definition of the coordinate directions.

In nuclear quadrupole resonance (NQR), we do not apply any static magnetic field and relies just on the quadrupole interaction. The resonance frequency for an NQR experiment for  $I = 3/2$  is given by the separation of the two eigenstates of eq.(2.6)

$$\nu_Q = \nu_Q^z \sqrt{1 + \eta^2/3} \quad (2.12)$$

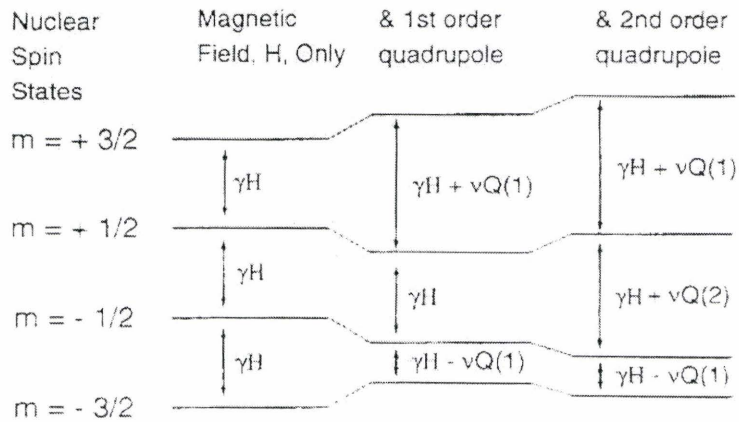
where z is the principle axis of the electric field gradient tensor.

For nuclear magnetic resonance (NMR), where a static magnetic field is applied, the quadrupole interaction is still present and changes the resonance frequencies from the purely magnetic Zeeman splitting. The first order perturbation effect does not change the central resonance frequency, but two satellite resonance splits off. On the other hand, second order perturbation even changes the central resonance frequency, as shown in the Figure 2.3.

### 2.2.3 Electronics

The NMR measurements presented in this thesis were conducted by the spectrometers which were constructed by previous group members (Kent Thurber and Allen Hunt) using commercially available components. The electronics, shown in block diagram in Figure 2.4, are required to accomplish two major tasks. First, it provides the pulsed R.F. that excites the nuclear spins in the sample and then the spin echo occurs. This requires careful timing and a pulse amplifier that provides peak to peak voltage of up to  $\sim 300$  V. Second, it needs to collect the extremely weak induced voltage signal from spin echo (on the order of  $\mu$  V), which requires a high gain system of amplifiers that connect to an analog to digital converter. The general flow of the

(a) NMR energy levels



(b) NMR resonance spectra

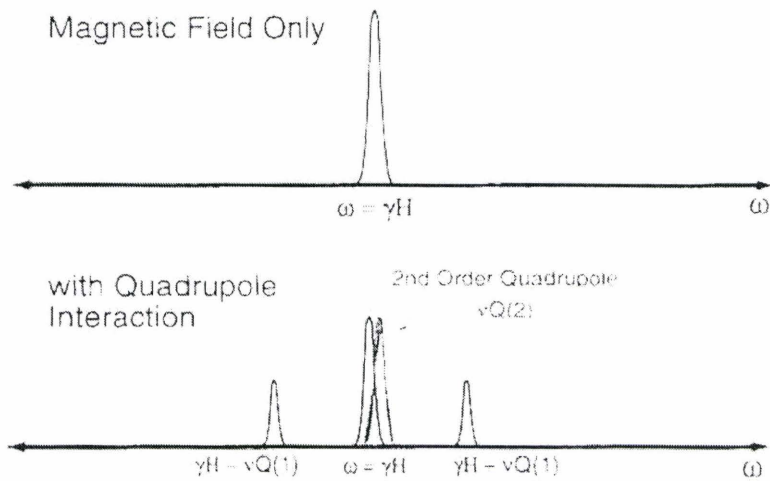


Figure 2.3 (a) Energy levels for NMR with spin  $I = \frac{3}{2}$  nucleus. (b) NMR resonance spectra for spin  $I = \frac{3}{2}$ .

electronics is outlined in the block diagram and is as follows.

1. The radio frequency (R.F.) sources (PTS 310 or 500) produces continuous R.F. from 1 - 500 MHz, which is gated into pulses by the TTL signals from the Aries spectrometer. The Aries is a product of TecMag company and controls all experimental timing and data acquisition, and is controlled by a Macintosh computer. These R.F. pulses pass through a home made protection circuit and are amplified by the power amplifier (Kalmus LP 1000, 1kW). The protection circuit contains simple logic elements and monitors several TTL lines to control the trigger line to the amplifier. The amplifier is engaged only for a brief time around the pulses and only when the logic of the protection circuit is satisfied. This prevents the accidental amplification of a large input signal, like continuous R.F., which could destroy the amplifier and fry precious samples. The amplified R.F. pulses are fed through paired diodes into NMR probe. The NMR probe consist of two adjustable capacitors and an inductive coil. This allows the circuit to be tuned to the chosen R.F. frequency and also matched to  $50 \Omega$  impedance. The sample is placed inside an coil and is subjected to the oscillating magnetic field created by the R.F. pulses, which manipulate the nuclear spins. The coil also detects the induced voltage from the spin echo.

2. The signal from spin echo need to be amplified and not influenced by the strong R.F. pulses or the ringdown that comes from the probe following the pulses, so a quarter wavelength cable and a pair of grounded crossed diodes are used. The voltage, which can be high at the probe, is at a minimum at the input side of the preamplifiers due to the quarter wavelength cable; while the crossed diodes short any large voltage (higher than the threshold  $\sim 0.6 \text{ V}$ ) to ground. Since the signal is small, it is unaffected by the diodes. These precautions are necessary to prevent the saturation of the signal amplifiers by the R.F. pulses, which would render the amplifiers useless when the actual signal arrives. The signal is then amplified by the cascaded signal

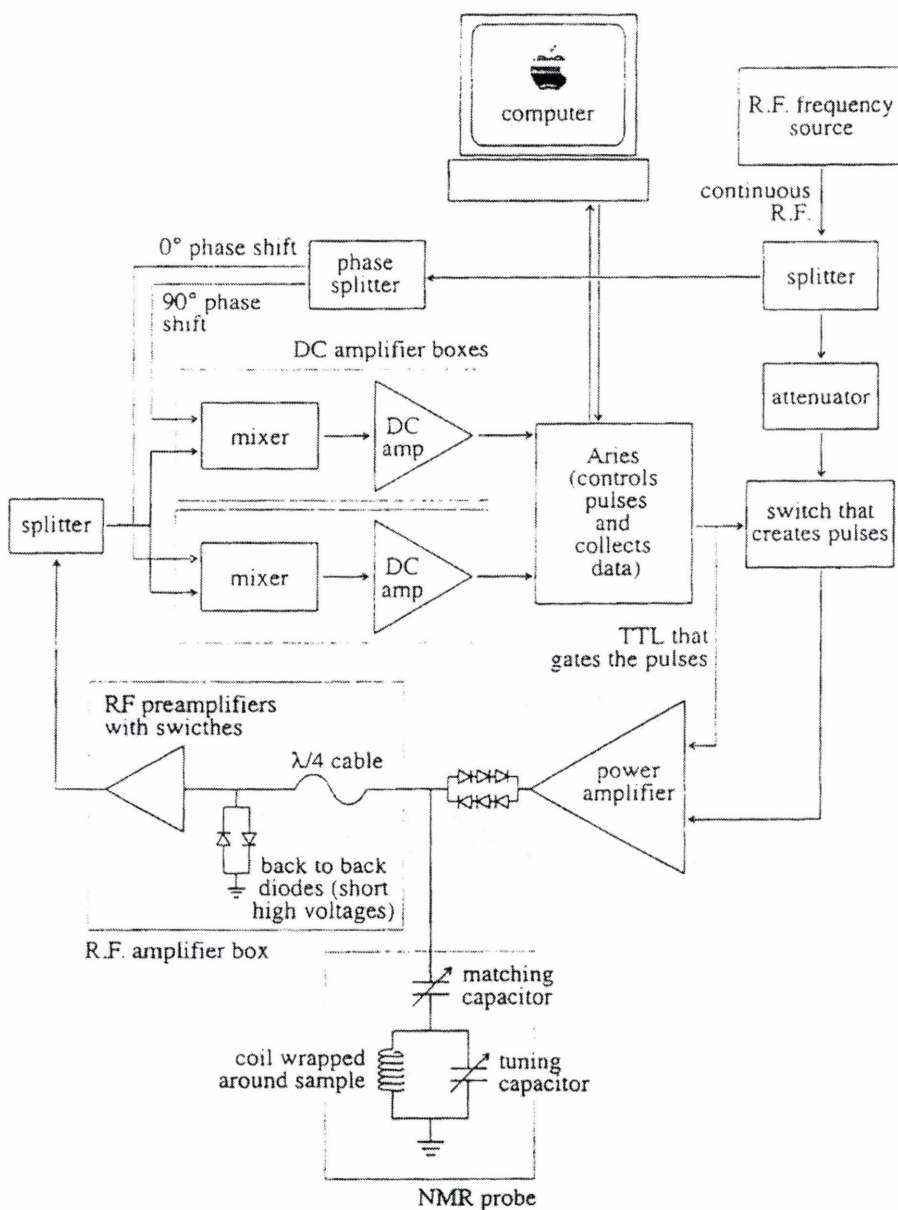


Figure 2.4 Schematic of electronics for NMR spectrometer, Imai labs.

amplifiers (LN-2M or LN-2L by Doty, or ZFL-500LN by Mini-Circuits). Generally, we have two Doty amplifiers which are separated by a pair of R.F. mixers (Mini-circuit ZAY-1B) which are used as switches. The switches are only turned on when we want to acquire the signal to avoid unnecessary saturation of the amplifiers. The signal is split and mixed with two copies of the original R.F. for the phase sensitive detection. One branch has been delayed by  $90^\circ$  by a phase splitter such as Mini-Circuits ZSQ-180B or by an appropriate length of added cable called a delay line. We monitor both phases with and without the  $90^\circ$  delay. This is referred to in the NMR literature as *quadrature detection*. Mixing with the two different phases essentially allows us to get both the cosine and sine components of the signal at the chosen frequency (or equivalently the real and imaginary parts). After mixing with the original R.F., the signal is close to DC ( we say it is DC because its frequency is much smaller than that of R.F.). We amplify the signal once more with an op-amp (AD521) based circuit with a gain of 100 and a complementary bandwidth of  $\sim 100$  kHz. This final signal can be viewed on an oscilloscope and is digitized by the analog to digital converter within the Aries. The analog to digital converter takes an input signal of -5 to +5 V, which is digitized into  $2^{12}$  bins. To take full advantage of this number of bins, we try to amplify the signal so that the noise is as big as a few volts. Less amplification results in a step problem between bins, which are now too large compared to the size of the noise and signal, while too much amplification would exceed the capabilities of the analog to digital converter. Additional NMR technique that is crucial for separation of the small spin echo signal from the decay (ringdown) of the R.F. pulses is phase cycling. In our resonant circuit ( $Q \sim 40-100$ ), the R.F. pulses require some time to decay and can obscure the spin echo signal. The pulse sequence are repeated with different phases for the R.F. pulses in order to cancel the decay of the R.F. pulse. For example, for the spin echo sequence, we use four different phases and add or subtract

the resulting signals based on the sign of the echo:

$$90_x \quad \tau \quad 180_x \quad \tau \quad echo_y \quad Add$$

$$90_{-x} \quad \tau \quad 180_x \quad \tau \quad echo_{-y} \quad Subtract$$

$$90_{-x} \quad \tau \quad 180_y \quad \tau \quad echo_y \quad Add$$

$$90_x \quad \tau \quad 180_y \quad \tau \quad echo_{-y} \quad Subtract$$

Where 90 and 180 refer to the 90 degree and 180 degree pulses with the subscript indicating the phase of the R.F. pulse. In this sequence, any ringdown of the 90 degree or 180 degree pulses is canceled. The phase cycling technique dramatically helps us to measure the spin echo at short  $\tau$ .

## 2.2.4 NMR Summary

In summary, NMR and NQR uses the atomic nuclei as local probes into materials. This thesis is primarily concerned with the ability of the nuclei to probe the electronic structure. The magnetic resonance frequency reveals the local uniform magnetic susceptibility,  $\chi(q = 0)$ . The quadrupole resonance frequency measures the electric field gradient, which reflects the charge environment.

# Chapter 3

## COBALT AND OXYGEN NMR RESULTS AND ANALYSIS

### 3.1 Contributions of NMR Community

In the excitement that followed the discovery of the new superconductor  $\text{Na}_{0.3}\text{CoO}_2\text{-}1.3\text{H}_2\text{O}$ , several NMR research groups began an intense study of this new material. Having provided valuable information on the BCS superconductors and High- $T_c$  cuprates, there was every reason to expect similar success with the new material. Before the new superconductor was discovered, several groups had measured  $^{59}\text{Co}$  NMR of the parent compound  $\text{Na}_{0.5}\text{CoO}_2$  (Ray et al., 1999, Itoh and Nagawatari, 2000). But these earlier works didn't have accurate calibration of the Na concentration and the actual Na concentration seems far from 0.5 as they claimed. Soon after the discovery of superconductor  $\text{Na}_{0.3}\text{CoO}_2\text{-}1.3\text{H}_2\text{O}$ , it was reported that the spin lattice relaxation rate for  $^{59}\text{Co}$  drops sharply in the superconducting state, indicating the absence of the coherence peak observed in BCS superconductors, therein the unconventional superconductivity (Fujimoto et al., 2004) .

Realizing the importance of studying the entire family of materials instead of just the superconducting members, our group was the first to present the  $^{59}\text{Co}$  line shapes, Knight shift, spin lattice relaxation rate for the whole family with Na concentration  $x$  range from 0.3 to 0.75 ( $x = 0.3, 0.5, 0.67, 0.72, 0.75$ ) (Ning et al., 2004). We concluded that there are two distinct types of Co sites (A site and B site) for  $x = 0.72$  and  $0.75$  and they are electronically coupled. We also concluded that Co valence averaged out in  $\text{Na}_{0.3}\text{CoO}_2$  and superconductor  $\text{Na}_{0.3}\text{CoO}_2-1.3\text{H}_2\text{O}$ . By  $^{17}\text{O}$  NMR experiment (Ning and Imai, 2005), We concluded that  $p-d$  hybridization induces sizable spin polarization in the oxygen triangular-lattice layers. Water intercalation makes  $\text{CoO}_2$  planes homogeneous and enhances low frequency spin fluctuations near  $T_c = 4.5$  K at some finite wave vectors, which are different from the ferromagnetic  $q = 0$  and frustrated  $q = (\frac{1}{3}, \frac{1}{3})$ .

In this thesis, I will focus on the experimental results and analysis of  $^{59}\text{Co}$  and isotope  $^{17}\text{O}$  for only three samples,  $\text{Na}_{0.72}\text{CoO}_2$ ,  $\text{Na}_{0.3}\text{CoO}_2$  and superconductor  $\text{Na}_{0.3}\text{CoO}_2-1.3\text{H}_2\text{O}$ .

## 3.2 Results and Analysis of $\text{Na}_{0.72}\text{CoO}_2$

### 3.2.1 $^{59}\text{Co}$ and $^{17}\text{O}$ NMR line shapes

For our  $^{59}\text{Co}$  and  $^{17}\text{O}$  NMR experiments, we used  $\text{Na}_{0.72}\text{CoO}_2$  and  $\text{Na}_{0.72}\text{Co}^{17}\text{O}_2$  powder sample, which I made by the solid state reaction method. Detailed procedures are described in Chapter 2. In order to make it easier to probe the electronic properties of the Co and Oxygen sites by NMR, we need an aligned sample. We ground the sample, and then mixed it with Stycast 1266 in a Teflon holder. Then we put the Teflon holder in a magnetic field of 8 Tesla. Since the magnetic susceptibility of  $\text{Na}_x\text{CoO}_2$  is

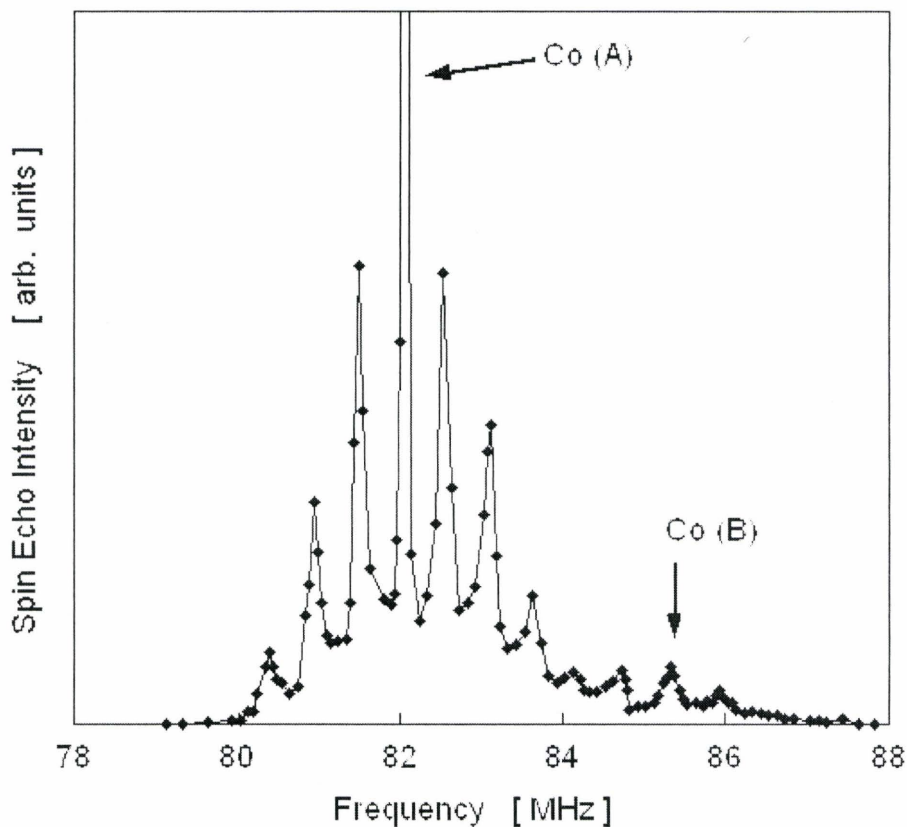


Figure 3.1  $^{59}\text{Co}$  NMR line shape of aligned ceramics  $\text{Na}_{0.72}\text{CoO}_2$  at 200 K with  $H_{ext}$  applied within the  $ab$  plane. The arrows indicate the central transition  $\nu_{-\frac{1}{2}, \frac{1}{2}}$  at two different sites. Some of the furthest satellite transitions are not shown above 88 MHz because  $^{23}\text{Na}$  NMR line was superposed.

larger along the ab plane than along the c axis (Chou et al., 2004a,b), the ab plane of ceramic particles will align themselves along the magnetic field. The orientation of the particles is fixed with the solidification of the Stycast 1266 overnight.

We applied an 8 Tesla magnetic field along the ab plane of the sample. By recording the NMR spin echo intensity obtained with a  $\frac{\pi}{2} - \tau - \pi$  pulse sequence versus frequency, we obtained  $^{59}\text{Co}$  and  $^{17}\text{O}$  NMR line shapes. Typical line shapes are shown in Figure 3.1 for Co sites and Figure 3.2 for oxygen sites. For  $^{59}\text{Co}$ , with a nuclear gyromagnetic ratio  $\gamma_n = 10.053 \text{ MHz/T}$ , the central resonance peak under 8 Tesla field is expected to be around 80.432 MHz. However, the nuclei also sense the magnetic properties of different Co sites, and the resonance has a Knight shift. At same time, since the  $^{59}\text{Co}$  nuclei have spin  $I = \frac{7}{2}$ , the resonance line splits to 7 peaks due to nuclear quadrupole interaction. In Figure 3.1, we can clearly see there are two different types of Co sites: one central resonance frequency (marked with A)  $\nu_{-\frac{1}{2}, \frac{1}{2}}$  is at 82 MHz; the other central resonance frequency (marked with B)  $\nu_{-\frac{1}{2}, \frac{1}{2}}$  is at 85.3 MHz. The quadrupole splitting of the resonance frequency  $\nu_a$  for both A site and B site are different too. e.g.,  $\nu_a \sim 500 \text{ kHz}$  at A site and  $\nu_a \sim 600 \text{ kHz}$  at B site. We integrated the NMR spin echo intensity between the A site and B site. The ratio is 0.72 : 0.28 within uncertainties, which is equal to the nominal molar ratio between  $\text{Co}^{+3}$  and  $\text{Co}^{+4}$  in the compound. We concluded that the electronic character of A site is close to less magnetic  $\text{Co}^{+3}$ -like ions with spin  $\sim 0$ , while the character of B site is close to strongly magnetic  $\text{Co}^{+4}$ -like ions with spin  $\sim \frac{1}{2}$ .

For  $^{17}\text{O}$ , with a nuclear gyromagnetic ratio  $\gamma_n = 5.772 \text{ MHz/T}$ , the central resonance peak under 8 Tesla field is expected to be around 46.172 MHz. Since  $^{17}\text{O}$  nuclear spin is  $I = \frac{5}{2}$ , the resonance frequency splits into five peaks. In Figure 3.2, we can see central resonance frequency of O(A) site  $\nu_{-\frac{1}{2}, \frac{1}{2}}$  is at 46.185 MHz with  $\nu_a = 95 \text{ kHz}$  and O(B) site  $\nu_{-\frac{1}{2}, \frac{1}{2}}$  is at 46.385 MHz with  $\nu_a = 95 \text{ kHz}$ . The integrated

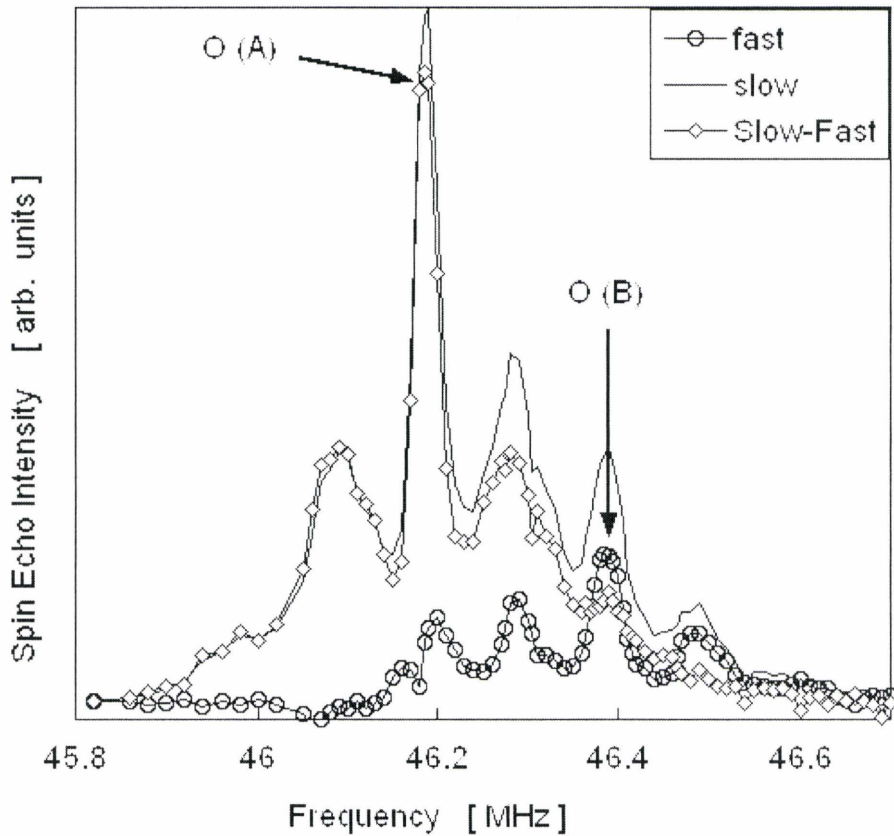


Figure 3.2  $^{17}\text{O}$  NMR line shape of aligned ceramics  $\text{Na}_{0.72}\text{Co}^{17}\text{O}_2$  at 77 K with  $H_{ext}$  applied within the ab plane. We applied an inversion pulse and waited for 2 msec before recording the spin echo intensity to separate the O(B) site with "fast" relaxation times. By taking the difference between the whole echo intensity ("slow") and the fast O(B) contributions ( $-\circ-$ ), we deduced the line shape of O(A) site ("difference"  $-\diamond-$ )

intensity ratio between O(A) site and O(B) site is also 0.72 : 0.28, which is same as the ratio between Co(A) site and Co(B) site.

### 3.2.2 Knight Shift

The Knight shift reflects the local magnetic susceptibility. The overall results are shown for  $^{59}\text{Co}$  Knight shift of  $\text{Na}_{0.72}\text{CoO}_2$  and  $^{17}\text{O}$  Knight shift of  $\text{Na}_{0.72}\text{Co}^{17}\text{O}_2$  in Figure 3.3 and Figure 3.4, respectively. As discussed in chapter 2 on NMR measurements, the orbital susceptibility and diamagnetic susceptibility are temperature independent in our present experiment temperature range (2 K  $\sim$  300K). The temperature dependent part of the Knight shift arises from the electron spins, and it is proportional to the uniform spin susceptibility (eq. 2.2). In Figure 3.3, the  $^{59}\text{Co}$  Knight shift of both A site and B site can be fitted to the Curie-Weiss law. This is consistent with the bulk susceptibility measured by SQUID. The lower panel shows the plot of Knight shift of Co(B) site versus that of Co(A) site, which can be fitted perfectly by a straight line. This plot indicates that the spin susceptibility of Co(A) site and Co(B) site have an identical temperature dependence, and they are electronically coupled. This result is not consistent with a simple phase separation picture as proposed by others (Carretta et al., 2004).

Oxygen Knight shift of both sites, as shown in Figure 3.4, can also be fitted to the Curie-Weiss law with a common Weiss temperature  $\theta \sim 27 \pm 2\text{K}$ . The A site Knight shift is also proportional to that of B site as shown by the straight line in the lower panel of Figure 3.4. Notice that the the magnitude of O(A) Knight shift is about 0.1%. While the Knight shift at the O(B) site is extraordinarily large and exceeds 1%, which is a order of magnitude larger than that of O(A). Likewise, the Co(B) sites exhibit a huge NMR Knight shift (up to 9%), while the Co(A) sites have

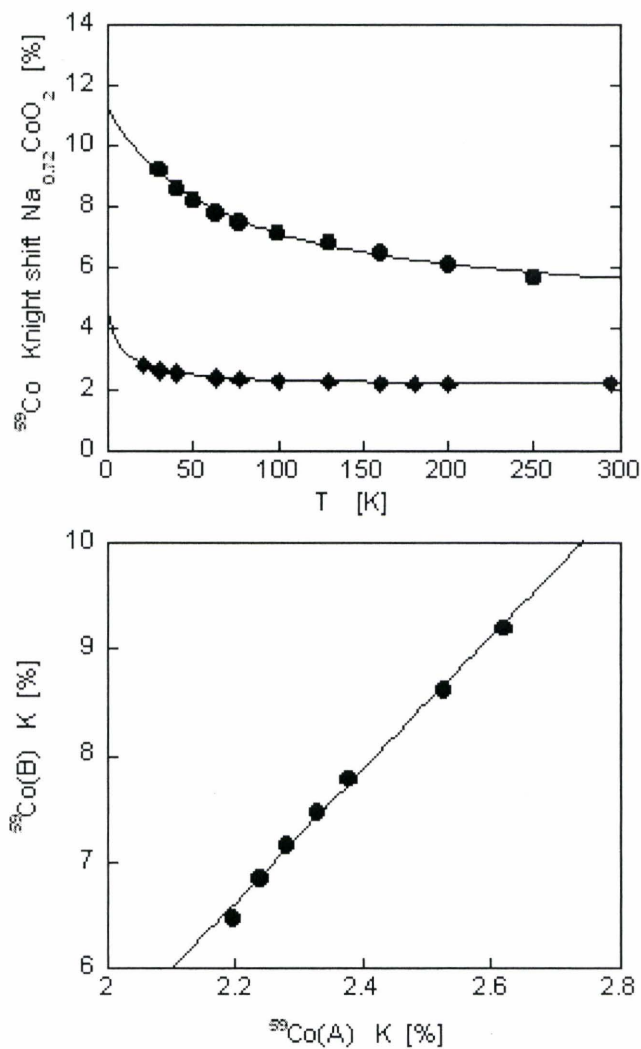


Figure 3.3 Upper panel:  $^{59}\text{Co}$  NMR Knight shift for Co(A) site ( $\blacklozenge$ ) and Co(B) site ( $\bullet$ ) with  $H_{ext}$  applied along ab-plane, solid lines are Curie-Weiss fit  $^{59}\text{K}(\text{A}) = 2.0884 + \frac{34.8}{T+27}$  (%) and  $^{59}\text{K}(\text{B}) = 5.335 + \frac{224.5}{T+28.6}$  (%). Lower panel: The Knight shift of Co(B) versus that of Co(A), the solid line is linear fit with a slope = 6.2.

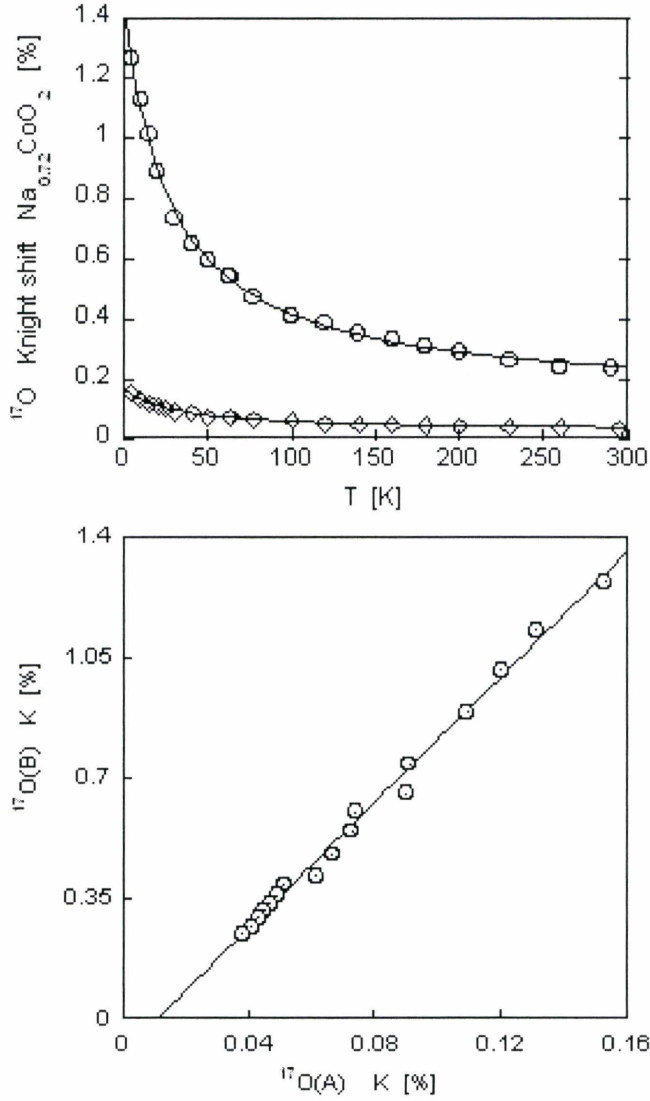


Figure 3.4 Upper panel:  $^{17}\text{O}$  NMR Knight shift for O(A) site ( $\diamond$ ) and O(B) site ( $\circ$ ) with  $H_{ext}$  applied along ab-plane, solid lines are Curie-Weiss fit  $^{17}\text{K}(A) = 0.02418 + \frac{4.3}{T+29.8}$  (%) and  $^{59}\text{K}(B) = 0.1298 + \frac{36.4}{T+27.3}$  (%). Lower panel: The Knight shift of O(B) versus that of O(A), the solid line is linear fit with a slope = 9.1.

nearly an order of magnitude smaller spin contribution. So the Knight shift data and the relative intensities of O(A) and O(B) sites strongly suggest that  $p$  orbital at the O(B) sites have a strong hybridization with the  $d$  orbital at the Co(B) sites, but the O(A) sites experience only mild effects from Co(B) sites. Notice that if each Co(B) site bonds equally with all six nearest neighbor O sites, the intensity of O(B) sites would be a factor of 3 larger and account for  $\sim 0.9$  of the total integrated intensity. Instead, our NMR results indicate that Co(B) sites transfer their spins primarily to one of the three nearest neighbor O sites in each of the O layers above and below the Co layers. This somewhat unexpected result should be taken into account in the debate over the magnetic interlayer coupling and the local symmetry of Co and O orbitals. For example, recent neutron scattering measurements (Bayrakci et al., 2005) showed that Co-Co interlayer exchange interactions in  $\text{Na}_{0.82}\text{CoO}_2$  are comparable to the intralayer exchange interactions despite its layered structure. There is no doubt that the similar Co(B)-O(B)-Na-O(B)-Co(B) exchange path is responsible for the unexpectedly large interlayer coupling.

### 3.2.3 The $K \sim \chi$ Plot

As discussed in chapter 2, we showed that the bulk magnetic susceptibility include three parts: the electron spin susceptibility,  $\chi_{spin}(q = 0)$  where  $q$  is the wave number; the electron orbital susceptibility (Van Vleck)  $\chi_{orbital}$ ; and the diamagnetic susceptibility  $\chi_{dia}$ . In our experiment temperature range, only the electron spin susceptibility is temperature dependent. Knight shift can be expressed as a linear function of electron spin susceptibility, as shown in eq.(2.3). The proportionality measures the hyperfine form factor  $A(q)$  at  $q = 0$ . Using the  $K - \chi$  plot analysis to compare the Knight shift and the bulk magnetic susceptibility, the hyperfine form factor may be

determined from eq.(2.4).

However, since there are two Co sites in  $\text{Na}_{0.72}\text{CoO}_2$ , the standard one-component relation between the Knight shift and the total bulk magnetic susceptibility eq.(2.3) and eq.(2.4) in chapter 2 does not hold any more. In order to separate individual  $\chi_{spin}(q=0)$ ,  $\chi_{orbital}$ ,  $\chi_{dia}$  contributions from the Co(A) site and Co(B) site, we need to make two assumptions. First, according to the results from NMR measurement of  $\text{Na}_1\text{CoO}_2$  (Lang et al., 2005, Vaulx et al., 2005), the total spins of  $\text{Co}^{+3} \sim 0$  and  $\text{Co}^{+3}$  sites are only very weakly magnetic. We assume that Co(A) sites have much smaller electron spin contributions  $\chi_{spin}(A, q=0)$  compared with that of Co(B) site,  $\chi_{spin}(B, q=0)$ , i.e.,

$$\chi_{spin}(B, q=0) \gg \chi_{spin}(A, q=0) \quad (3.1)$$

Secondly, we ignore the Knight shift part from diamagnetic susceptibility, since this contribution is so small compared with the  $K_{orbital}$ . This will not affect the value of spin contribution for the Knight shift. Under those two assumptions, the total observed Knight shift can be expressed by

$$K_{obv}^A = K_{spin}^A + K_{vv}^A \quad (3.2)$$

$$K_{obv}^B = K_{spin}^B + K_{vv}^B \quad (3.3)$$

The total observed bulk magnetic susceptibility as measured with SQUID can be expressed by

$$\chi_{obv} = \chi_{dia} + \chi_{vv}^{total} + \chi_{spin}^{total} = \chi_{dia} + \chi_{vv}^A + \chi_{vv}^B + \chi_{spin}^A + \chi_{spin}^B \quad (3.4)$$

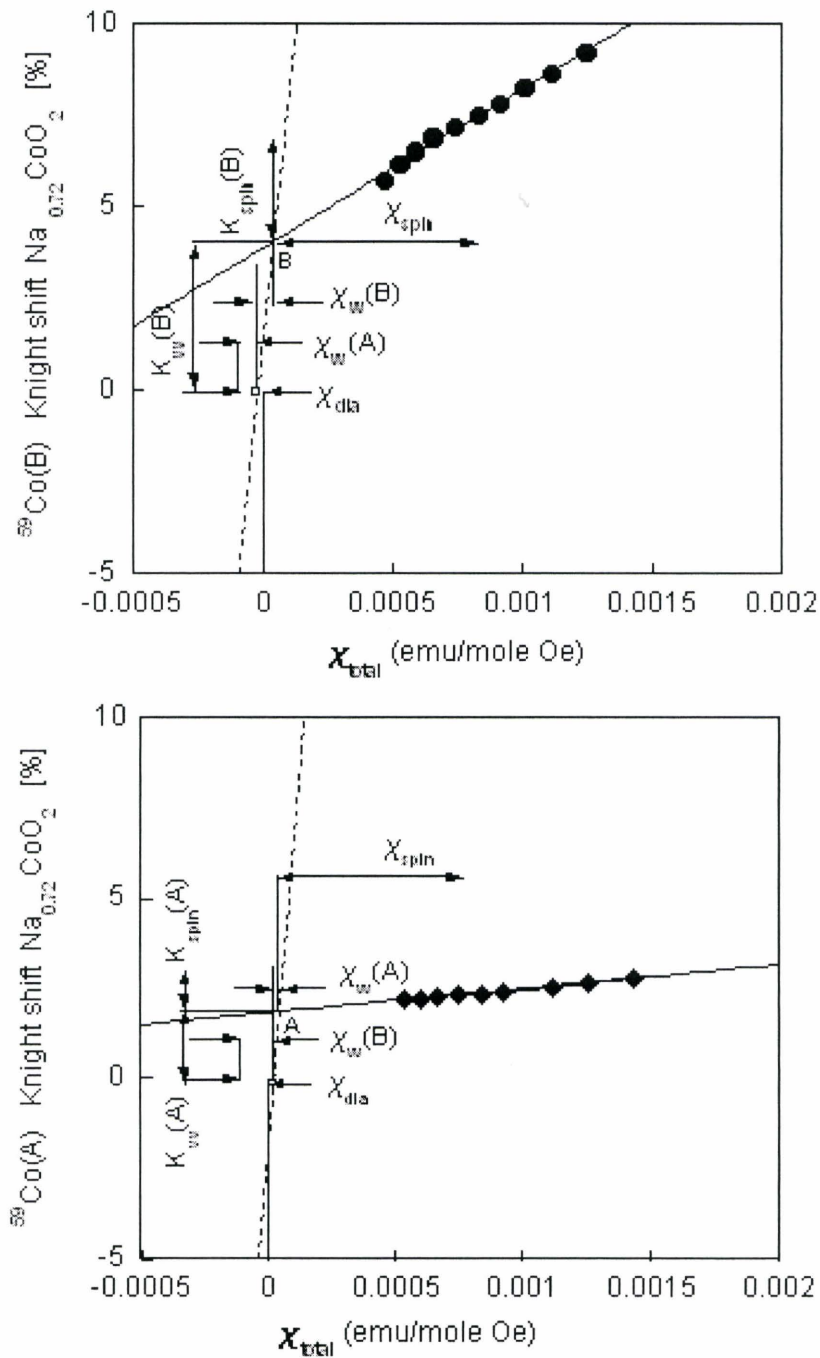


Figure 3.5  $^{59}\text{Co}$  Knight shift versus bulk magnetic susceptibility  $\chi$  plot of  $\text{Na}_{0.72}\text{CoO}_2$ . Notice that point A and B should have same x-axis coordinate.

Notice that,

$$\chi_{vv}^{total} = \chi_{vv}^A + \chi_{vv}^B \quad (3.5)$$

is a constant number and with the supposition eq. 3.1, the total observed magnetic susceptibility can be expressed as

$$\chi_{obv} = \chi_{dia} + \chi_{vv}^{total} + \chi_{spin}^B \quad (3.6)$$

The total diamagnetic susceptibility is a summation of the diamagnetic susceptibilities for ions which are some known numbers (Gupta, 1986) such as  $\chi_{dia}^{Na^+} = -5 \times 10^{-6}$  emu/mole Oe;  $\chi_{dia}^{Co^{+3}} = -10 \times 10^{-6}$  emu/mole Oe;  $\chi_{dia}^{Co^{+4}} = -5 \times 10^{-6}$  emu/mole Oe;  $\chi_{dia}^{H^+} = 0 \times 10^{-6}$  emu/mole Oe;  $\chi_{dia}^{O^{2-}} = -12 \times 10^{-6}$  emu/mole Oe. The total diamagnetic susceptibilities of  $Na_{0.72}CoO_2 = -37.068 \times 10^{-6}$  emu/mole Oe, as described in the Figure 3.5.

First, we look at the upper panel of Figure 3.5. The hyperfine coupling constant of the orbital moment for Co(B) sites,  $A_{vv}(B) = \frac{K_{vv}^B}{\chi_{vv}^B} = 6.75 \times 10^2$  kOe/ $\mu_B$  was estimated as a product of  $\langle \frac{1}{r^3} \rangle = 5.4$  a.u. for  $Co^{+4}$  (Blazey and Müller, 1983). The coupling constants for the temperature dependent Knight shift of Co(B) sites A(B,  $q = 0$ ) was estimated as  $2.4051 \times 10^2$  kOe/ $\mu_B$  by the least linear fitting shown as solid line in the upper panel of Figure 3.5. Obviously, known the parameters from the fitting, the solid line can be expressed by a linear function.

By taking  $\chi_{dia} + \chi_{vv}^A$  as the starting point, which is shown as an open circle, we drew a dashed line with slope equal to  $A_{vv}(B)$ . This dashed line can be expressed by a linear function in terms of the unknown factor  $\chi_{vv}^A$ . This dash line intercepts with the solid line in point B. We marked the coordinates of point B as  $(x(B), y(B))$ . Obviously, the value of  $x(B)$  and  $y(B)$  can be expressed in terms of the unknown

factor  $\chi_{vv}^A$ . Notice that we can also obtain,

$$\chi_{vv}^B = x(B) - (\chi_{dia} + \chi_{vv}^A) \quad (3.7)$$

Second, in the same way, as shown in the lower panel of Figure 3.5, the hyperfine coupling constant of the orbital moment for Co(A) sites,  $A_{vv}(A) = \frac{K_{vv}^A}{\chi_{vv}^A} = 8.375 \times 10^2 \text{ kOe}/\mu_B$  was estimated as a product of  $\frac{1}{\langle r^{-3} \rangle} = 6.7 \text{ a.u.}$  for  $\text{Co}^{+3}$ . The coupling constants for the temperature dependent Knight shift of Co(A) sites  $A(A, q = 0)$  is estimated as  $0.37614 \times 10^2 \text{ kOe}/\mu_B$  by the least fitting shown as solid line. The solid line can be expressed to be a linear function by knowing the fitting parameters. We took  $\chi_{dia} + \chi_{vv}^B$  as the starting point, which is also shown as an open circle, and drew a dashed line with slope equal to  $A_{vv}(A)$ . Now this dashed line can be expressed by a linear function in terms of the unknown factor  $\chi_{vv}^B$ . This dash line intercepts with the solid line in point A. We marked the coordinates of point A as  $(x(A), y(A))$ . In the same way, the value of  $x(A)$  and  $y(A)$  can be expressed in terms of the unknown factor  $\chi_{vv}^B$ . Notice that here, we can also obtain,

$$\chi_{vv}^A = x(A) - (\chi_{dia} + \chi_{vv}^B) \quad (3.8)$$

Combining eq. 3.7 and eq. 3.8 together, we can see  $x(A) = x(B)$ . Then we can completely calculate and separate  $\chi_{vv}^A$  and  $\chi_{vv}^B$ . The values derived are shown in the second column in Table 3.1.

Bring  $\chi_{vv}^A$  back to the linear function of the dashed line in the upper panel, we can calculate  $y(B)$ . The magnitude of  $y(B)$  is the value of  $K_{orbital}(B)$ , which is 4.0255 %. The Knight shift above  $y(B)$  are  $K_{spin}(B)$ , which is at least 1.5 %, as shown in the graph. In the same way, bring  $\chi_{vv}^B$  back to the linear function of the dashed line in the

lower panel, we can calculate  $y(A)$ . The magnitude of  $y(A)$  is the value of  $K_{orbital}(A)$ , which is 1.816 %. The Knight shift above  $y(A)$  are  $K_{spin}(A)$ , which are about 0.2 %, as shown in the graph. All values derived are shown in the second column in Table 3.1.

So far, we have been assuming that Co(A) site is exactly  $Co^{+3}$ , and Co(B) site is exactly  $Co^{+4}$ . Now let's consider another possibility: the valences of  $Co^{+3}$  and  $Co^{+4}$  in  $Na_{0.72}CoO_2$  are averaged out, i.e., the Co valence is +3.28. We take the hyperfine coupling constant for the orbital moment,  $A_{vv}(A,B) = \frac{K_{vv}^{A,B}}{\chi_{vv}^{A,B}} = 7.8875 \times 10^2 \text{ kOe}/\mu_B$ . This value was estimated as a product of  $\frac{1}{\langle r^3 \rangle} (average) = 6.336 \text{ a.u.}$ , which is weighted the average value of  $\frac{1}{\langle r^3 \rangle} = 6.7 \text{ a.u.}$  for  $Co^{+3}$  and  $\frac{1}{\langle r^3 \rangle} = 5.4 \text{ a.u.}$  for  $Co^{+4}$ . Then we use the same method as shown above to do calculations. The results are shown in the third column in Table 3.1. Notice that the second column values and third column values are comparable. Compared with the values estimated directly from Curie-Weiss fit as shown in fourth column, we find that the orbital Knight shift are almost the same within the error bar. This strongly suggests that above assumptions are reasonable and acceptable. Also, two scenarios of Co valence do not give very different results. However, if we compared the total orbital magnetic susceptibility

Table 3.1 Values from  $K \sim \chi$  plot for Co sites of  $Na_{0.72}CoO_2$

	$A_{vv}^A = 837.5, A_{vv}^B = 675$	$A_{vv}^A, A_{vv}^B$ averaged	Curie-Weiss fit
$K_{vv}^A$ (%)	1.816	1.81078	2.0884
$K_{vv}^B$ (%)	4.0255	3.99217	4.4047
$\chi_{vv}^A$ (emu/moleOe)	2.16842e-5	2.29576e-5	41.48e-5( $\chi_{vv}^{total}$ )
$\chi_{vv}^B$ (emu/moleOe)	5.96375e-5	5.06139e-5	
$\chi_{dia}$ (emu/moleOe)	-3.7068e-5	-3.7068e-5	-3.7068e-5
$A(A, q=0) \text{ kOe}/\mu_B$	37.614	37.614	
$A(B, q=0) \text{ kOe}/\mu_B$	240.51	240.51	

$\chi_{vv}^{total} = \chi_{vv}^A + \chi_{vv}^B \sim 8 \times 10^{-6}$  emu/mole Oe from the  $K \sim \chi$  plot with the value from the Curie-Weiss fit ( $41.5 \times 10^{-6}$  emu/mole Oe), there is still a factor of 5 difference. This may be attributed to the temperature-independent contributions of Co(A) site since we ignored the spin contributions of the Co(A) site above.

### 3.3 Results and Analysis of $\text{Na}_{0.3}\text{CoO}_2$

#### 3.3.1 Line shapes and Knight Shift

For the  $^{59}\text{Co}$  NMR experiment, we used a single crystal of  $\text{Na}_{0.3}\text{CoO}_2$ , which was grown by F.C.Chou at MIT. Laue x-ray scattering was used to confirm the directions of the crystal axes in the sample. We applied an 8 Tesla magnetic field along the c-axis of the sample. By recording the NMR spin echo intensity obtained with a  $\frac{\pi}{2} - \tau - \pi$  pulse sequence versus frequency, we obtained the  $^{59}\text{Co}$  line shapes. Typical line shape is shown in Figure 3.6 for the Co site. We can see that the background is very low and clean, which indicates the high quality and homogeneity of the crystal. In contrast to the line shapes of  $\text{Na}_{0.72}\text{CoO}_2$ , we have detected essentially only one class of  $^{59}\text{Co}$  NMR lines in this metallic material. The central resonance frequency  $\nu_{-\frac{1}{2}, \frac{1}{2}}$  is at 81.9 MHz and other six satellite resonance peaks symmetrically arranged around it with  $\nu_c \sim 4$  MHz by quadrupole interaction. Combining with the Knight shift shown in the inset of Figure 3.6 and  $T_1$  measurements (not shown here), we concluded that the valence of all Co ions in the ground state of  $\text{Na}_{0.3}\text{CoO}_2$  are averaged out. There is only one type of Co site. However, we can not rule out the possibility that changes in the nature and extent of  $\text{Na}^+$  vacancy order may be driving the changes of electronic properties across  $x = 0.5$  from  $\text{Na}_{0.72}\text{CoO}_2$  to  $\text{Na}_{0.3}\text{CoO}_2$ .

For the  $^{17}\text{O}$  NMR experiment, we used a powder sample prepared by myself.

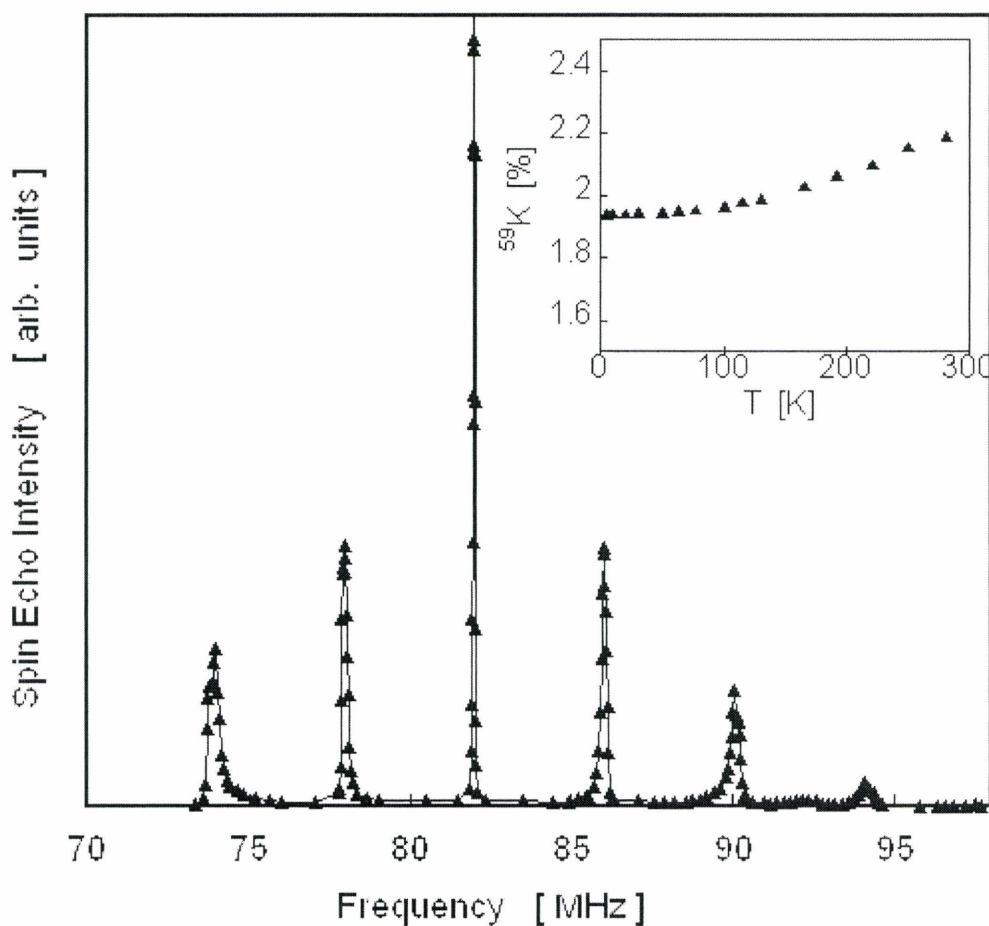


Figure 3.6 Main panel:  $^{59}\text{Co}$  line shape of single crystal  $\text{Na}_{0.3}\text{CoO}_2$  at 4.2 K with  $H_{ext}$  applied parallel to the c-axis.  $\nu_c \sim 4$  MHz. Inset:  $^{59}\text{Co}$  NMR Knight shift of single crystal  $\text{Na}_{0.3}\text{CoO}_2$  with  $H_{ext}$  applied parallel to the c-axis.

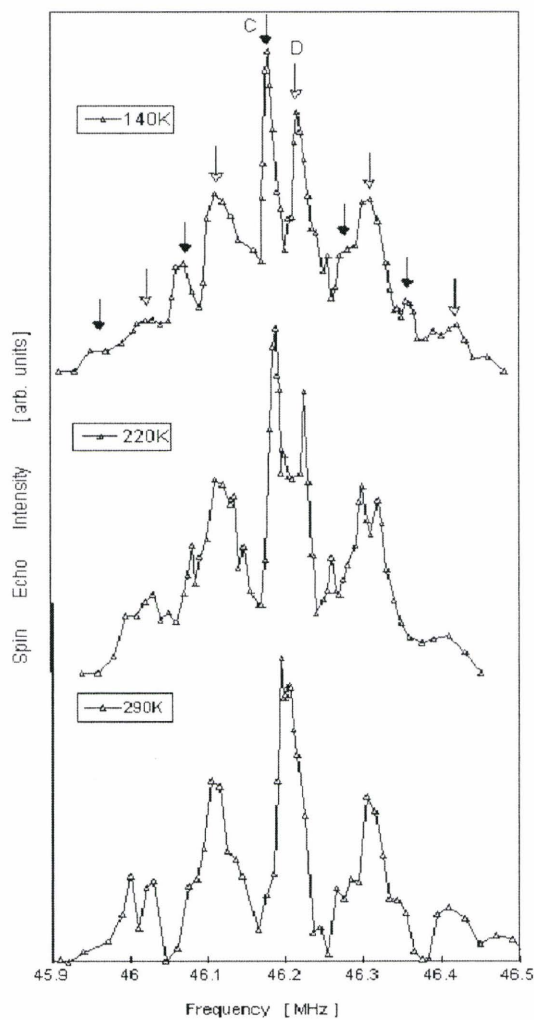


Figure 3.7  $^{17}\text{O}$  line shapes of aligned ceramics  $\text{Na}_{0.35}\text{CoO}_2$  with  $H_{ext}$  applied within the  $ab$  plane. O(C) site (filled arrows) merge with O(D) site (open arrows) to a single line with temperature increasing.

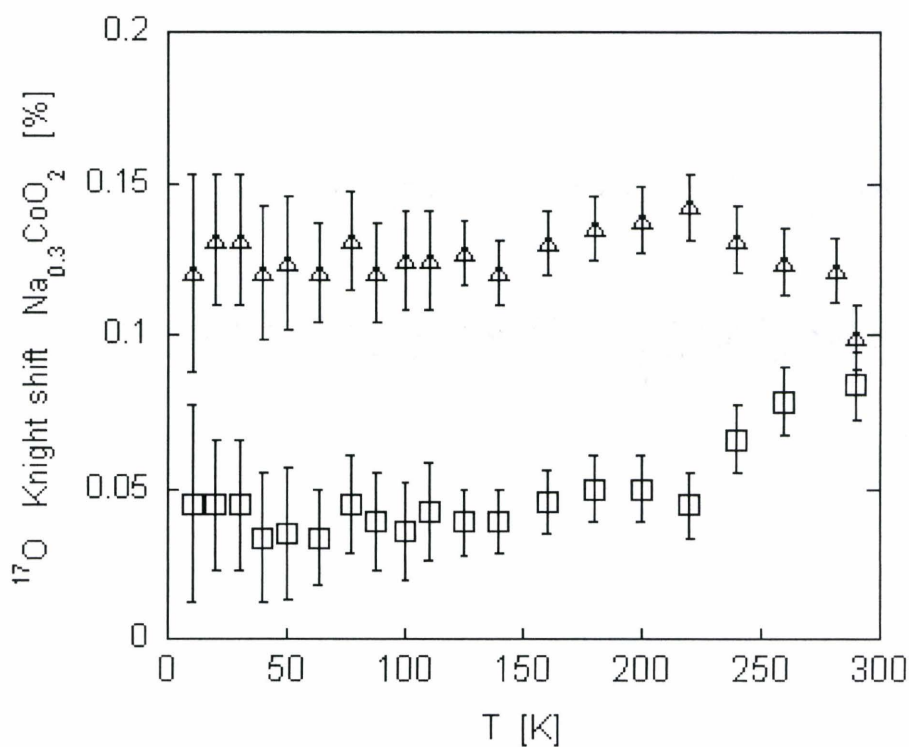


Figure 3.8  $^{17}\text{O}$  NMR Knight shift for O(C) site ( $\square$ ) and O(D) site ( $\triangle$ ) with  $H_{ext}$  applied along ab-plane. The Knight shifts of both sites are same at 295 K due to motion narrowing effect.

The detailed procedures are described in chapter 2. We characterized the sample by powder X-ray diffraction and confirmed the concentration  $x \sim 0.35 \pm 0.04$ . We aligned the powder sample in Stycast 1266 in a magnetic field of 8 Tesla. Typical NMR line shapes are shown in Figure 3.7. Examining the line shape on top, which was measured at 140 K, we see that there are two types of  $^{17}\text{O}$  sites, we called them O(C) site and O(D) site. The center transition frequency  $\nu_{-\frac{1}{2},\frac{1}{2}}$  of O(C) site is at 46.178 MHz and  $\nu_c \sim 100$  kHz. The center transition frequency  $\nu_{-\frac{1}{2},\frac{1}{2}}$  of O(D) site is at 46.215 MHz and also  $\nu_c \sim 100$  kHz. Two sites have roughly comparable intensities. Unlike the large difference of intensity for O(A) site and O(B) site in  $\text{Na}_{0.72}\text{CoO}_2$ , the difference in the local electronic environment at O(C) and O(D) sites is small. This is consistent with our finding from the Co NMR studies that the tendency toward charge differentiation is strongly suppressed in the Fermi liquid phase. With the temperature increasing, the O(C) site and O(D) site merge to a single line, as shown shown in Figure 3.7, the line shapes at 220 K and 290 K. This is the *motion narrowing* effect due to the thermal motion of  $\text{Na}^+$  ions above 220 K. This suggests that O(C) and O(D) sites are differentiated by the occupancy of  $\text{Na}^+$  sites nearby.

Let's look at the Knight shift of  $^{59}\text{Co}$  and  $^{17}\text{O}$  in Figure 3.6 and Figure 3.8. We can see that both  $^{59}\text{K}$  and  $^{17}\text{O}$  show a slight decrease with temperature down to 100 K, and leads to a constant value below 100 K. This finding suggests Pauli paramagnetic susceptibility and is evidence for the emergence of low-temperature canonical Fermi-liquid behavior. This is also consistent with the emergence of  $\sim T^2$  behavior of resistivity observed only for  $x \sim \frac{1}{3}$  below  $\sim 30$  K (Foo et al., 2004).

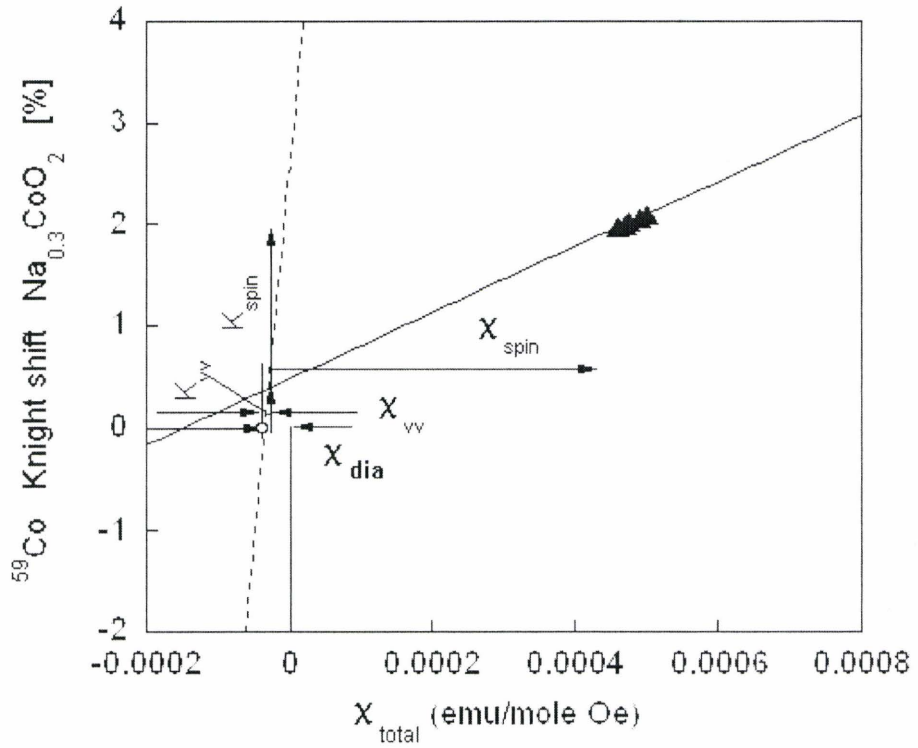


Figure 3.9  $^{59}\text{Co}$  Knight shift with  $H_{\text{ext}}$  along c-axis versus bulk magnetic susceptibility  $\chi$  plot of  $\text{Na}_{0.35}\text{CoO}_2$ .

### 3.3.2 The $K \sim \chi$ Plot

We used only Knight shift above 100 K to do  $K$  vs  $\chi$  plot analysis (as shown in Figure 3.9) since only this part has temperature dependence. Because there is only one Co site in  $\text{Na}_{0.3}\text{CoO}_2$  with  $H_{ext}$  along  $c$ -axis, the  $K \sim \chi$  plot become straightforward as discussed in Chapter 2. The total diamagnetic susceptibility of  $\text{Na}_{0.3}\text{CoO}_2$  is  $-34.17 \times 10^{-6}$  emu/mole Oe according to the summation of the known diamagnetic susceptibilities of ions, as shown in section 3.2.3. As discussed above, the Co valence averaged out in this compound, i.e., the Co valence is +3.7. We took the hyperfine coupling constant for the orbital moment,  $A_{vv} = \frac{K_{vv}}{\chi_{vv}} = 7.2375 \times 10^2$  kOe/ $\mu_B$ . This value was estimated as a product of  $\frac{1}{\langle r^3 \rangle} (average) = 5.79$  a.u., which is the weighted average value of  $\frac{1}{\langle r^3 \rangle} = 6.7$  a.u. for  $\text{Co}^{+3}$  and  $\frac{1}{\langle r^3 \rangle} = 5.4$  a.u. for  $\text{Co}^{+4}$ . The coupling constants for the temperature dependent Knight shift of Co site A( $q = 0$ ) is estimated as  $1.8105 \times 10^2$  kOe/ $\mu_B$  by the least fitting shown as solid line. We took  $\chi_{dia}$  as the starting point, which is shown as an open circle, and drew a dashed line with slope equal to  $A_{vv}$ . This dashed line intercepts with the solid line. Then we can easily determine  $\chi_{vv} = 5.346 \times 10^{-6}$  emu/mole Oe;  $K_{vv} = 0.38694$  %;  $K_{spin} \sim 1.5$  %.

## 3.4 Results and Analysis of $\text{Na}_{0.3}\text{CoO}_2-1.3\text{H}_2\text{O}$

### 3.4.1 Line shapes and Knight Shift

The  $^{59}\text{Co}$  NMR line shape was measured from the fully hydrated superconducting crystal sample  $\text{Na}_{0.3}\text{CoO}_2-1.3\text{H}_2\text{O}$ , which was prepared by sealing the crystal sample  $\text{Na}_{0.3}\text{CoO}_2$  in a water vapor saturated container at room temperature for several months to fully hydrate this mm-size single crystal. Neutron diffraction on a superconducting crystal revealed that the sample is single phase ( $> 90$  % of the

sample, within the errors) with a c-axis lattice constant of 19.65 Å at room temperature (Chou et al., 2004a,b). We applied 8 Tesla magnetic field along ab plane of the crystal, and obtained  $^{59}\text{Co}$  line shapes by recording the NMR spin echo intensity obtained with a  $\frac{\pi}{2} - \tau - \pi$  pulse sequence versus frequency. The typical  $^{59}\text{Co}$  line shape of  $\text{Na}_{0.3}\text{CoO}_2-1.3\text{H}_2\text{O}$  is shown in Figure 3.10. There is only one Co site in the superconducting sample with the central transition  $\nu_{-\frac{1}{2},\frac{1}{2}}$  at 83.3 MHz and  $\nu_{ab} \sim 1.85$  MHz, the broad satellite peaks are due to the different  $\nu_Q$  along a-direction and b-direction.

To obtain superconducting sample  $\text{Na}_{0.3}\text{Co}^{17}\text{O}_2-1.3\text{H}_2\text{O}$ , we soaked some portion of  $^{17}\text{O}$  enriched  $\text{Na}_{0.35}\text{CoO}_2$  ceramics in purified water for several days. We verified that for  $^{59}\text{Co}$ , the  $\pm \frac{7}{2}$  to  $\pm \frac{5}{2}$  nuclear quadrupole resonance (NQR) frequency  $^{59}\nu_{NQR} = 12.3$  MHz and  $^{59}1/T_1T_{NQR} = 18 \text{ sec}^{-1}\text{K}^{-1}$  observed just above  $T_c$  agree very well with earlier reports (Fujimoto et al., 2004, Ihara et al., 2005). We used unaligned ceramics of  $\text{Na}_{0.3}\text{CoO}_2-1.3\text{H}_2\text{O}$  under an 8 Tesla magnetic field for NMR measurements because alignment with Stycast 1266 tends to reduce water content and damage superconducting properties. Typical  $^{17}\text{O}$  line shape is shown in Figure 3.11. In contrast with  $\text{Na}_{0.3}\text{Co}^{17}\text{O}_2$ , there is only one oxygen site in the superconducting sample, with the central transition frequency  $\nu_{-\frac{1}{2},\frac{1}{2}}$  at 46.195 MHz and  $\nu_Q \sim 80$  kHz. This means that the O-layers are electronically homogenous in the superconducting phase.

The Knight shift of  $^{59}\text{Co}$  and  $^{17}\text{O}$  are shown in Figure 3.12. Within the error bar, both of them are temperature independent below 100 K down to  $T_c$ . Combined with our spin-lattice relaxation  $1/T_1T$  measurements, we rule out the possibility of ferromagnetic scenario of spin excitations above  $T_c$ . Since there is only one Co site and one O site in superconducting sample, the K vs  $\chi$  plot becomes straightforward. The  $^{59}\text{Co}$  K vs  $\chi$  plot is shown in Figure 3.13. The total diamagnetic susceptibility of  $\text{Na}_{0.3}\text{CoO}_2$  is  $-49.77 \times 10^{-6} \text{ emu/mole Oe}$  according to the summation of the known

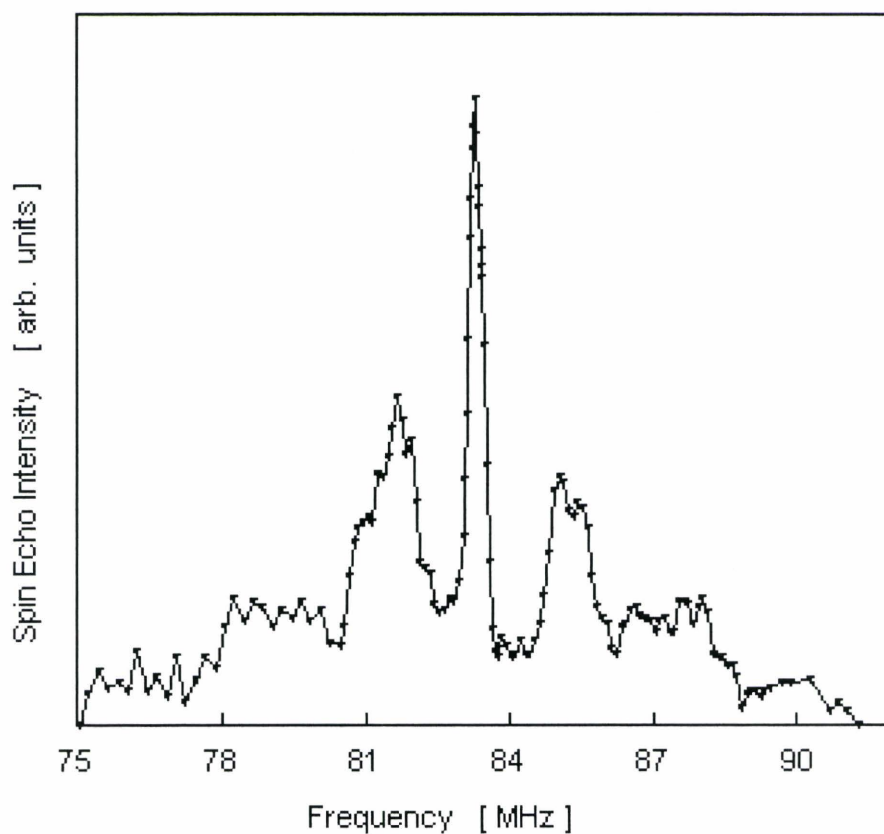


Figure 3.10  $^{59}\text{Co}$  NMR line shape of single crystal  $\text{Na}_{0.3}\text{CoO}_2 \cdot 1.3\text{H}_2\text{O}$  at 77 K with  $H_{ext}$  applied within the  $ab$  plane.  $\nu_{ab} \sim 1.85$  MHz.

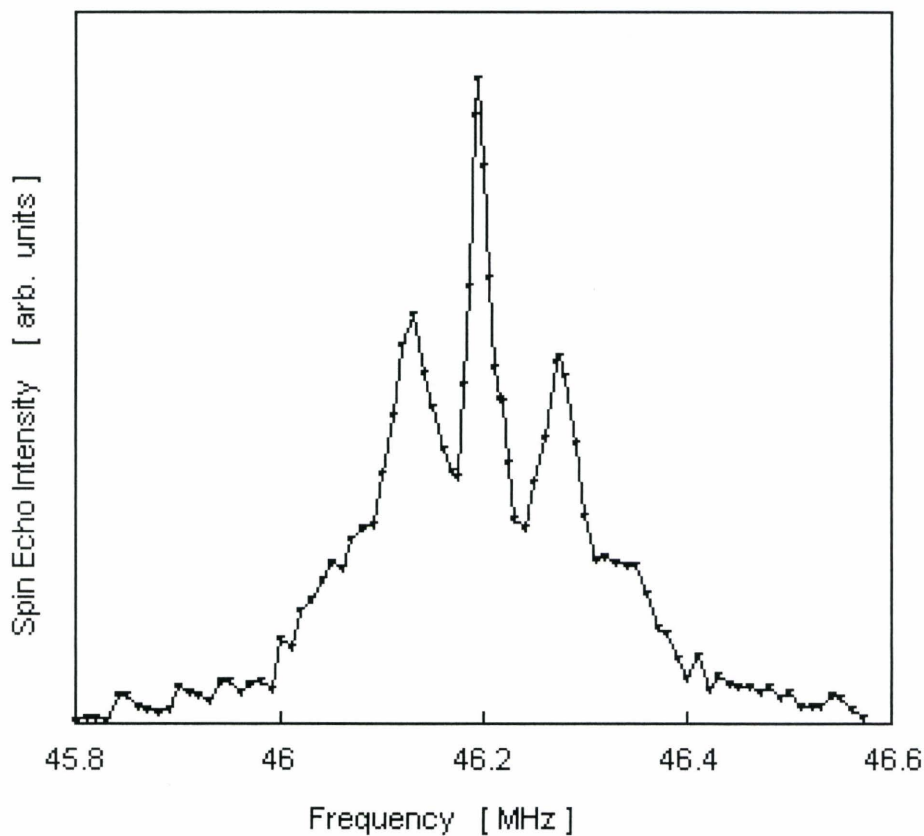


Figure 3.11 The powder pattern  $^{17}\text{O}$  NMR line shapes of  $\text{Na}_{0.35}\text{CoO}_2-1.3\text{H}_2\text{O}$  ceramics at 77 K. The less pronounced peak structures and the high and low frequency tails are due to random orientations of the sample.

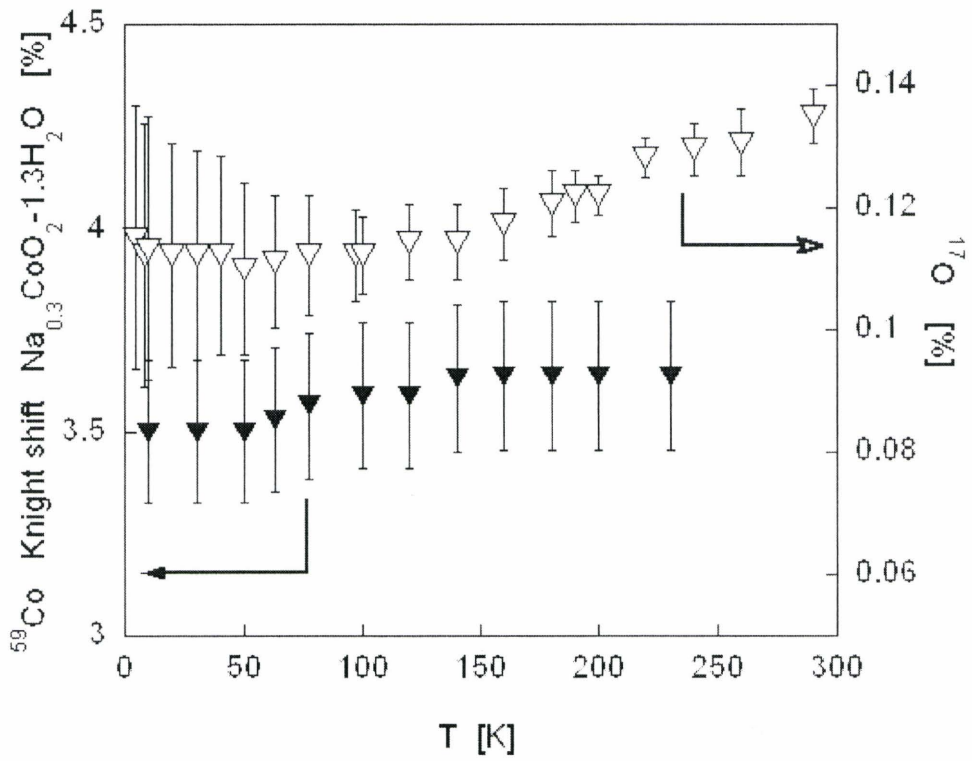


Figure 3.12  $^{59}\text{Co}$  NMR Knight shift( ▼ ) of single crystal  $\text{Na}_{0.3}\text{CoO}_2-1.3\text{H}_2\text{O}$  with  $H_{ext}$  applied parallel to the ab-plane and  $^{17}\text{O}$  NMR Knight shift( ▽ ) of unaligned ceramics  $\text{Na}_{0.3}\text{Co}^{17}\text{O}_2-1.3\text{H}_2\text{O}$ .

diamagnetic susceptibilities of ions, as shown in section 3.2.3. Because Co valence averaged out in this compound as discussed above, we took the hyperfine coupling constant for the orbital moment,  $A_{vv} = \frac{K_{vv}}{\chi_{vv}} = 7.2375 \times 10^2 \text{ kOe}/\mu_B$ , same as that of  $\text{Na}_{0.3}\text{CoO}_2$ . The coupling constants for the temperature dependent Knight shift of Co site A(Co,  $q = 0$ ) is estimated as  $1.8783 \times 10^2 \text{ kOe}/\mu_B$  by the least fitting shown as the solid line. We take  $\chi_{dia}$  as the starting point, which is shown as an open circle, and draw a dashed line with slope equal to  $A_{vv}$ . This dashed line intercepts with the solid line. Then we can obtain  $\chi_{vv} = 33.786 \times 10^{-6} \text{ emu/mole Oe}$ ;  $K_{vv} = 2.445 \%$ ;  $K_{spin} \sim 1.5 \%$ .

For the oxygen K vs  $\chi$  plot, the coupling constants for the temperature dependent Knight shift of O site A(O,  $q = 0$ ) is estimated as  $11.651 \text{ kOe}/\mu_B$  by a least fitting shown as the solid line. We take  $\chi_{dia} + \chi_{vv}(Co)$  as the starting point, which is shown as an open circle in Figure 3.14, and draw a vertical dashed line. This dashed line intercept with the solid line. Then we can determine  $K_{vv} = 0.04435 \%$ ,  $K_{spin} \sim 0.06 \%$ , as shown in Figure 3.14.

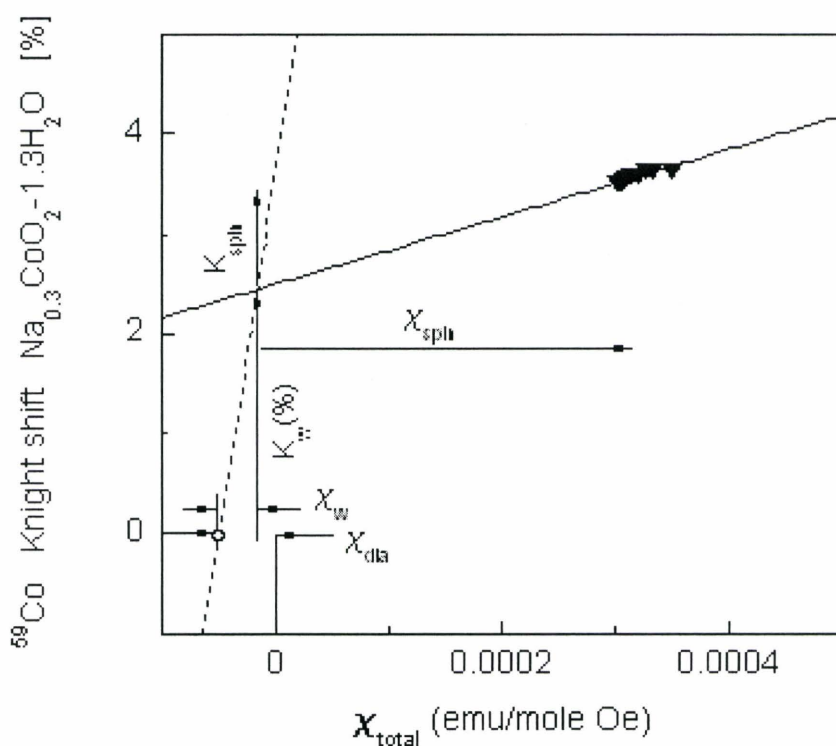


Figure 3.13  $^{59}\text{Co}$  Knight shift with  $H_{\text{ext}}$  along ab plane versus bulk magnetic susceptibility  $\chi$  plot of  $\text{Na}_{0.3}\text{Co}^{17}\text{O}_2-1.3\text{H}_2\text{O}$ .

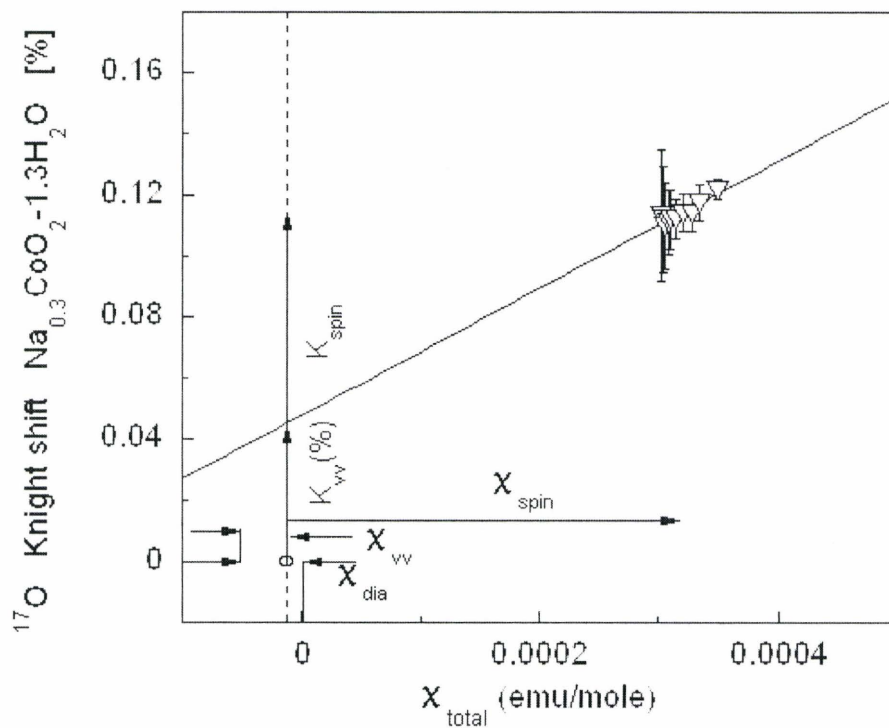


Figure 3.14  $^{17}\text{O}$  Knight shift with  $H_{ext}$  along ab plane versus bulk magnetic susceptibility  $\chi$  plot of  $\text{Na}_{0.3}\text{Co}^{17}\text{O}_2-1.3\text{H}_2\text{O}$ .

# Chapter 4

## CONCLUSION

We investigated the local electronic properties of the triangular-lattice materials  $\text{Na}_x\text{CoO}_2$  ( $x = 0.3, 0.72$ ) and the superconductor  $\text{Na}_{0.3}\text{CoO}_2 \cdot 1.3\text{H}_2\text{O}$  by  $^{59}\text{Co}$  and  $^{17}\text{O}$  Nuclear Magnetic Resonance.

For  $\text{Na}_{0.72}\text{CoO}_2$ ,  $^{59}\text{Co}$  NMR line shape shows clearly that there are two types of Co sites – Co(A) site and Co(B) site. The ratio of the integrated spin echo intensity between Co(A) site and Co(B) site is  $0.72 : 0.28$  within uncertainties, which is equal to the molar ratio between  $\text{Co}^{+3}$  and  $\text{Co}^{+4}$  in this material. This ratio is also equal to that of occupied and vacant  $\text{Na}^+$  sites. We conclude that the electronic character of the Co(A) site is close to the less magnetic  $\text{Co}^{+3}$ -like ion with spin  $\sim 0$ , while the electronic character of the Co(B) site is close to the strongly magnetic  $\text{Co}^{+4}$ -like ions with spin  $\sim \frac{1}{2}$ . We emphasize that the valence of Co(A) and Co(B) sites is not necessarily equal to +3 and +4, precisely. The temperature dependence of the Knight shifts suggests that the Co(A) site and Co(B) site are electronically coupled, which is not consistent with simple phase separation. Consequently, there are two types of oxygen sites – O(A) site and O(B) site with relative integrated spin echo intensity of  $\sim 0.7$  and  $\sim 0.3$ . This indicates that the local Co electronic environments propagate

to the adjacent O layers through p-d hybridization. Along the ab-plane, K vs  $\chi$  plot determined that for Co sites,  $K_{orbital}(A)$  is 1.816 % and  $K_{spin}(A)$  is about  $\sim 0.2$  %;  $K_{orbital}(B)$  is 4.0255 % and  $K_{spin}(B)$  are at least 1.5 %.

For  $\text{Na}_{0.3}\text{CoO}_2$ ,  $^{59}\text{Co}$  NMR line shape shows that there is only one type of Co site, which means that Co valence is averaged out in this material. On the other hand, there are two types of oxygen sites O(C) site and O(D) site presumably because of the nearest neighbor  $\text{Na}^+$  sites. The constant behavior of the Knight shifts below 100 K for both Co site and O sites suggests the emergence of a low temperature canonical Fermi-liquid behavior. Along the c-axis, from the K vs  $\chi$  plot, we determined that for Co site,  $K_{orbital}$  is 0.387 % and  $K_{spin}$  is about  $\sim 1.5$  %.

For the superconductor  $\text{Na}_{0.3}\text{CoO}_2\cdot 1.3\text{H}_2\text{O}$ , both  $^{59}\text{Co}$  and  $^{17}\text{O}$  NMR line shapes show that there is only one type of Co site and oxygen site. The Knight shifts of  $^{59}\text{Co}$  and  $^{17}\text{O}$  are temperature independent below 100 K down to  $T_c$ . Combined with our spin-lattice relaxation  $1/T_1T$  measurements, we rule out the possibility of ferromagnetic scenario of spin excitations above  $T_c$ . Along the ab-plane, we showed that for Co site,  $K_{orbital}$  is 2.445 % and  $K_{spin}$  is about  $\sim 1.5$  %; For the oxygen site,  $K_{orbital}(O)$  is 0.04435 % and  $K_{spin}(O)$  is about  $\sim 0.06$  %.

# References

- Abragam, A. (1961). *Principle of Nuclear Magnetism*. Oxford Univeristy Press, Oxford.
- Anderson, P. W. (1987). *Science*, 235, 1196.
- Ashcroft, N. W. and Mermin, N. D. (1976). *Solid State Physics*. Harcourt Brace, Fort Worth.
- Bardeen, J., Cooper, L. N., and Schrieffer, J. R. (1957). *Phys. Rev.*, 108, 1175.
- Bayrakci, S. P., Mirebeau, I., Bourges, P., Sidis, Y., Enderle, M., Mesot, J., Chen, D. P., Lin, C. T., and Keimer, B. (2005). *Phys. Rev. Lett*, 94, 157205.
- Bednorz, J. G. and Müller, K. A. (1986). *Z. Phys. B*, 64, 189.
- Blazey, K. W. and Müller, K. A. (1983). *J. Phys. C: Solid State Phys.*, 16, 5491.
- Carretta, P., Mariani, M., Azzoni, C. B., and Mozzati, M. C. (2004). *Phys. Rev. B*, 70, 024409.
- Chou, F. C., Cho, J. H., Lee, P. A., Abel, E. T., Matan, K., and Lee, Y. S. (2004a). *Phys. Rev. Lett*, 92, 157004.
- Chou, F. C., Cho, J. H., and Lee, Y. S. (2004b). *Phys. Rev. B*, 70, 144526.

- Foo, M. L., Wang, Y. Y., Watauchi, S., Zandbergen, H. W., He, T., Cava, R. J., and Cava, N. P. (2004). *Phys. Rev. Lett.*, 92, 247001.
- Fujimoto, T., Zheng, G. Q., Kitaoka, Y., Meng, R. L., Cmaidalka, J., and Chu, C. W. (2004). *Phys. Rev. Lett.*, 92, 047004.
- Gavilano, J. L., Rau, D., Pedrini, B., Hinderer, J., Ott, H. R., Kazakov, S. M., and Karpinski, J. (2004). *Phys. Rev. B*, 69, 100404R.
- Gupta, R. R. (1986). *Landolt-Börnstein*, volume 16 of *II*. Springer-Verlag, Berlin Heidelberg New York London Paris Tokyo.
- Huang, Q., Foo, M. L., R. A. Pascal, J., Lynn, J. W., Toby, B. H., He, T., Zandbergen, H. W., and Cava, R. J. (2004a). *Phys. Rev. B*, 70, 184110.
- Huang, Q., Khaykovich, B., Chou, F. C., Cho, J. H., Lynn, J. W., and Lee, Y. S. (2004b). *Phys. Rev. B*, 70, 134115.
- Ihara, Y., Ishida, K., Michioka, C., Kato, M., Yoshimura, K., Takada, K., Sasaki, T., Sakurai, H., and Takayam-Muromachi, E. (2005). *J. Phys. Soc. Jpn.*, 74(3), 867.
- Itoh, M. and Nagawatari, M. (2000). *Physica B (Amsterdam)*, 281-282, 516.
- Jaccarino, V. (1966). *Proc. of Int. School of Physics, Enrico Fermi*, volume 37. Academic Press.
- Jorgensen, J. D., Avdeev, M., Hinks, D. G., Burley, J. C., and Short, S. (2003). *Phys. Rev. B*, 68, 214517.
- Kittel, C. (1996). *Introduction to Solid State Physics*. John Wiley and Sons, New York, 7th edition.

- Lang, G., Bobroff, J., Alloul, H., Mendels, P., Blanchard, N., and Collin, G. (2005). *Phys. Rev. B*, 72, 094404.
- Lynn, J. W., Huang, Q., Brown, C. M., Miller, V. L., Foo, M. L., Schaak, R. E., Jones, C. Y., Mackey, E. A., and Cava, R. J. (2003). *Phys. Rev. B*, 68, 214516.
- Milne, C. J., Argyriou, D. N., Chemseddine, A., Aliouane, N., Veira, J., Landsgesell, and Alber, D. (2004). *Phys. Rev. Lett.*, 93, 247007.
- Motohashi, T., Naujalis, E., Ueda, R., Isawa, K., Karppinen, M., and Yamauchi, H. (2001). *Appl. Phys. Lett.*, 79, 1480.
- Motohashi, T., Ueda, R., Naujalis, E., Tojo, T., Terasaki, I., Atake, T., Karppinen, M., and Yamauchi, H. (2003). *Phys. Rev. B*, 67, 064406.
- Ning, F. L. and Imai, T. (2005). *Phys. Rev. Lett*, 94, 227004.
- Ning, F. L., Imai, T., Statt, B. W., and Chou, F. C. (2004). *Phys. Rev. Lett*, 93, 237201.
- Ray, R., Ghoshray, A., Ghoshray, K., and Nakamura, S. (1999). *Phys. Rev. B*, 59, 9454.
- Sakurai, H., Takenouchi, S., Tsujii, N., and Takayama-Muromachi, E. (2004a). *J. Phys. Soc. Jpn.*, 73(8), 2081.
- Sakurai, H., Tsujii, N., and Takayama-Muromachi, E. (2004b). *J. Phys. Soc. Jpn.*, 73(8), 2393.
- Sales, B. C., Jin, R., Affholter, K. A., Khalifah, P., Veith, G. M., and Mandrus, D. (2004). *Phys. Rev. B*, 70, 174419.

- Slichter, C. P. (1990). *Principles of Magnetic Resonance*. Springer-Verlag, New York.
- Takada, K., Fukuda, K., Osada, M., Nakai, I., Izumi, F., Dilanian, R. A., Kato, K., Takata, M., Sakurai, H., Takayama-Muromachi, E., and Sasaki, T. (2004). *J. Mater. Chem*, 14, 1448.
- Takada, K., Sakurai, H., Takayama-Murumachi, E., Izumi, F., Dilanian, R. A., and Sasaki, T. (2003). *Nature*, 53, 422.
- Terasaki, I., Sasago, Y., and Uchinokura, K. (1997). *Phys. Rev. B*, 56, R12685.
- Vaulx, C. D., Julien, M. H., Berthier, C., Horvatic, M., Bordet, P., Simonet, V., Chen, D. P., and Lin, C. T. (2005). *Phys. Rev. Lett*, 95, 186405.